

JGR Solid Earth

RESEARCH ARTICLE

10.1029/2022JB024265

Key Points:

- Coeval dilational hydroshear veins and mylonites may shed light on deformation mechanisms of deep episodic tremor and slow slip events
- Dilational hydroshear veins formed by incremental crack-seal at supralithostatic pore pressure values and deformed by dislocation creep
- Blueschist facies mylonites formed mainly by a combination of dissolution-precipitation creep and slip along phyllosilicate bands

Supporting Information:

Supporting Information may be found in the online version of this article.

Correspondence to:

F. Giuntoli,
francesco.giuntoli@unibo.it

Citation:

Giuntoli, F., Viola, G., & Sørensen, B. E. (2022). Deformation mechanisms of blueschist facies continental metasediments may offer insights into deep episodic tremor and slow slip events. *Journal of Geophysical Research: Solid Earth*, 127, e2022JB024265. <https://doi.org/10.1029/2022JB024265>



Received 22 FEB 2022

Accepted 2 OCT 2022

© 2022. The Authors.

This is an open access article under the terms of the [Creative Commons Attribution License](https://creativecommons.org/licenses/by/4.0/), which permits use, distribution and reproduction in any medium, provided the original work is properly cited.

Deformation Mechanisms of Blueschist Facies Continental Metasediments May Offer Insights Into Deep Episodic Tremor and Slow Slip Events

Francesco Giuntoli¹ , Giulio Viola¹ , and Bjørn Eske Sørensen² 

¹Department of Biological, Geological and Environmental Sciences, Università degli Studi di Bologna, Bologna, Italy,

²Department of Geoscience and Petroleum, Norwegian University of Science and Technology, Trondheim, Norway

Abstract Exhumed fossil subduction zones are archives of the deformation conditions and mechanisms from depths not directly accessible. Microstructural analysis of samples exhumed therefrom offers insights into the micromechanics and deformation processes associated with subduction such as earthquakes, slow earthquakes, and aseismic creep. Subducted and exhumed continental metasediments of the Tuscan Metamorphic Units of the Italian Northern Apennines contain a mylonitic foliation and quartz and carpholite dilational hydroshear veins with crack-and-seal textures, both developed at blueschist facies conditions (350–400°C, ~1 GPa). As shown by overprinting relationships and mineral assemblages, these two structure types formed broadly coeval within the stability field of carpholite. Metaconglomerates and metaquartzarenites deformed mainly by dissolution-precipitation creep and secondary by dislocation creep. Microstructural and electron backscatter diffraction analyses of the veins suggest only limited recrystallization of quartz fibers by subgrain rotation recrystallization, with adjacent metapelite bands acting as decollement horizons, likely by slip on the basal plane of phyllosilicates. We estimated differential stresses of 43–55 MPa and strain rates between 10^{-13} and 10^{-14} s⁻¹ from the vein recrystallized quartz fibers. We propose these microstructures and deformation mechanisms to represent a geological evidence of deep episodic tremor and slow slip events in subducted continental metasediments. Pore pressure cyclically reached supralithostatic values triggering tremors causing fracturing of all involved lithotypes. Likely, slow slip was accommodated preferentially by slip on phyllosilicate bands. Aseismic creep occurred mainly by dislocation creep with subgrain rotation recrystallization in vein quartz, slip on the basal plane of phyllosilicates, and dissolution and precipitation creep in the host rock.

Plain Language Summary Rocks exhumed from great depth can help us to investigate processes otherwise non directly accessible. The Italian Northern Apennines comprise exhumed continental sediments that were deformed and metamorphosed at depths of 30–40 km and temperatures of 350–400°C. Broadly coeval continuous and discontinuous deformation is documented as highly deformed zones (shear zones) and veins. We used microstructural analyses and electron microscopy techniques to reconstruct how these rocks deformed and the structures formed. Quartz-rich metasediments deformed mainly by dissolution and precipitation processes. Weak phyllosilicate-rich bands accommodated deformation likely by slip on their platy basal planes. Fluid pressure cyclically reached high values that caused failure of the metasediments, with subsequent migration of portion of the fluid and formation of the veins. Veins display only a limited amount of crystal plastic deformation. Quartz paleopiezometry and flow law suggest low differential stresses and average geological strain rates for the deformation of veins. We propose that these structures can be seen as a possible geological record of deep episodic tremor and slow slip events, low intensity and long lasting seismic events associated with slip transients faster than average plate motion.

1. Introduction

The spectrum of seismic activity modes associated with subduction zones comprises at the one end megathrust earthquakes characterized by high moment magnitudes, high slip rates, strain rates and stress drops ($M_w \sim 7\text{--}9.2$, 10^0 m s⁻¹, $>10^0$ s⁻¹, ~0.4–100 MPa; Bilek & Lay, 2018; Kirkpatrick et al., 2021; Lingling et al., 2021) and, at the other, episodic tremor and slow slip events (ETS) characterized by lower moment magnitudes, slip rates, strain rates, and stress drops (M_w 5.3?–6.7, $\sim 10^{-7}\text{--}10^{-6}$ m s⁻¹, $10^{-10}\text{--}10^0$ s⁻¹, 1–100 kPa; Behr & Bürgmann, 2021; Kirkpatrick et al., 2021). Tremors are low-amplitude seismic signals associated with slow slip, that is, slip

transients greater than the average plate motion (e.g., Beroza & Ide, 2011; Gomberg & the Cascadia 2007 and Beyond Working Group, 2010; Ito et al., 2007). ETS are associated with high ratios of the *P*-wave and *S*-wave velocities related to high pore pressure that can cyclically exceed lithostatic values (e.g., Audet et al., 2009; Kato et al., 2010; Saffer & Tobin, 2011). ETS are believed to be capable to dissipate up to between 75% and 100% of the stress related to convergence along the plate interface in subduction zones below 25 km depth (Chapman & Melbourne, 2009; Wallace & Beavan, 2010). Some studies propose a spatial and temporal relationship between ETS and megathrust earthquakes (Obara & Kato, 2016), although some debate still exists (Gao & Wang, 2017).

While the geophysical expression of ETS is detected in the geophysical record of several active subduction zones, the geological record of ETS (if any) is less obvious and only suggestions have so far been made from the study of geological structures of a few fossil subduction settings formed under a wide spectrum of geothermal gradients. ETS occur both at the up- (shallow ETS) and down-dip limit (deep ETS) of the locked seismogenic zone (review in Behr & Bürgmann, 2021; Gomberg & Group, 2010; Kirkpatrick et al., 2021; Obara, 2020). While the potential recorded evidence of shallow ETS is relatively accessible in nature and can also be directly investigated by deep drillings into the shallow parts of accretionary wedges (Barnes et al., 2020), this is not the case for deep ETS, which remain deeper than ~25 km. Their potential tangible record, therefore, can only be studied in deeply exhumed fossil subduction zones and be used as an analogue of modern subduction zones. In turn, such an approach becomes crucial to a refined interpretation of modern geophysical and geodetic data.

The few studies that so far have investigated deformation structures potentially ascribable to deep ETS report structures formed in response to alternating continuous and discontinuous deformation associated with high pore pressure in compositionally heterogeneous rock sequences (summary in Behr & Bürgmann, 2021; Kirkpatrick et al., 2021). In detail, these structures include foliated cataclaste or breccia and veins mutually crosscutting with the surrounding mylonitic foliation (Angiboust et al., 2015; Malatesta et al., 2018; Muñoz-Montecinos et al., 2020, 2021). Other diagnostic features include rheologically stronger blocks embedded in a weaker matrix. In particular, at Syros Island (Greece) metabasites contain eclogite lenses surrounded by a blueschist facies foliation (Behr et al., 2018; Kotowski & Behr, 2019). Dilational hydroshear veining during coeval ductile deformation is also commonly described from rocks deformed at conditions similar to those dominant at the ETS source region (Fagereng et al., 2010; Ujiie et al., 2018). Veins formed under those conditions are reported to contain fibrous minerals and to exhibit crack-and-seal textures, with fluid inclusion bands marking successive growth increments (e.g., Cox & Etheridge, 1983; Koehn & Passchier, 2000; Raimbourg et al., 2021). It has been proposed that these structures represent also a fossil analogue of deep ETS in continental metasediments subducted to blueschist facies conditions (for the Italian Northern Apennines by Giuntoli & Viola, 2021, 2022).

Even fewer studies characterize in detail the brittle and crystalloplastic microstructures and deformation mechanisms possibly associated with deep ETS. For example, eclogite lenses display evidence of deformation by brittle shear fractures and veins, whereas the blueschist facies foliation deformed by dislocation creep (Behr et al., 2018; Kotowski & Behr, 2019). Metasediments display evidence of crenulation and dilational microcracking alternating with dissolution-precipitation creep and limited dislocation creep in quartz-rich layers (Platt et al., 2018; W. L. Schmidt & Platt, 2022). Metagranitoids display a switch in deformation mechanisms from brittle deformation and ductile deformation at blueschist facies conditions related to fluctuation of pore pressure (Molli et al., 2017).

Here we contribute filling this knowledge gap by presenting for the first time a detailed microstructural study of blueschist facies mylonites and associated dilational hydroshear veins from rocks potentially recording ETS. The rocks studied from a microstructural point of view in this work were recently used by Giuntoli and Viola (2021, 2022) to describe the petrotectonic evolution of mylonites and dilational hydroshear veins and to constrain their metamorphic conditions in the broader framework of the Northern Apennines subduction history. In this article we take a step further by analyzing key and representative microstructures with electron backscatter diffraction and by inferring the main deformation mechanisms that accommodated strain in these rocks. This original dataset helps to document that quartz fibers in dilational hydroshear veins with crack-and-seal textures only recorded little deformation by dislocation creep and subgrain rotation recrystallization, while the intervening phyllosilicate-rich bands acted as small-scale decollement horizons likely by slip on the basal plane of phyllosilicates. We present evidence for dissolution-precipitation creep as a major deformation mechanism in the host metaconglomerate and metarenite. Finally, we propose a conceptual model for the deformation mechanisms of deep ETS and discuss the role of lithological heterogeneities in the development of deep ETS.

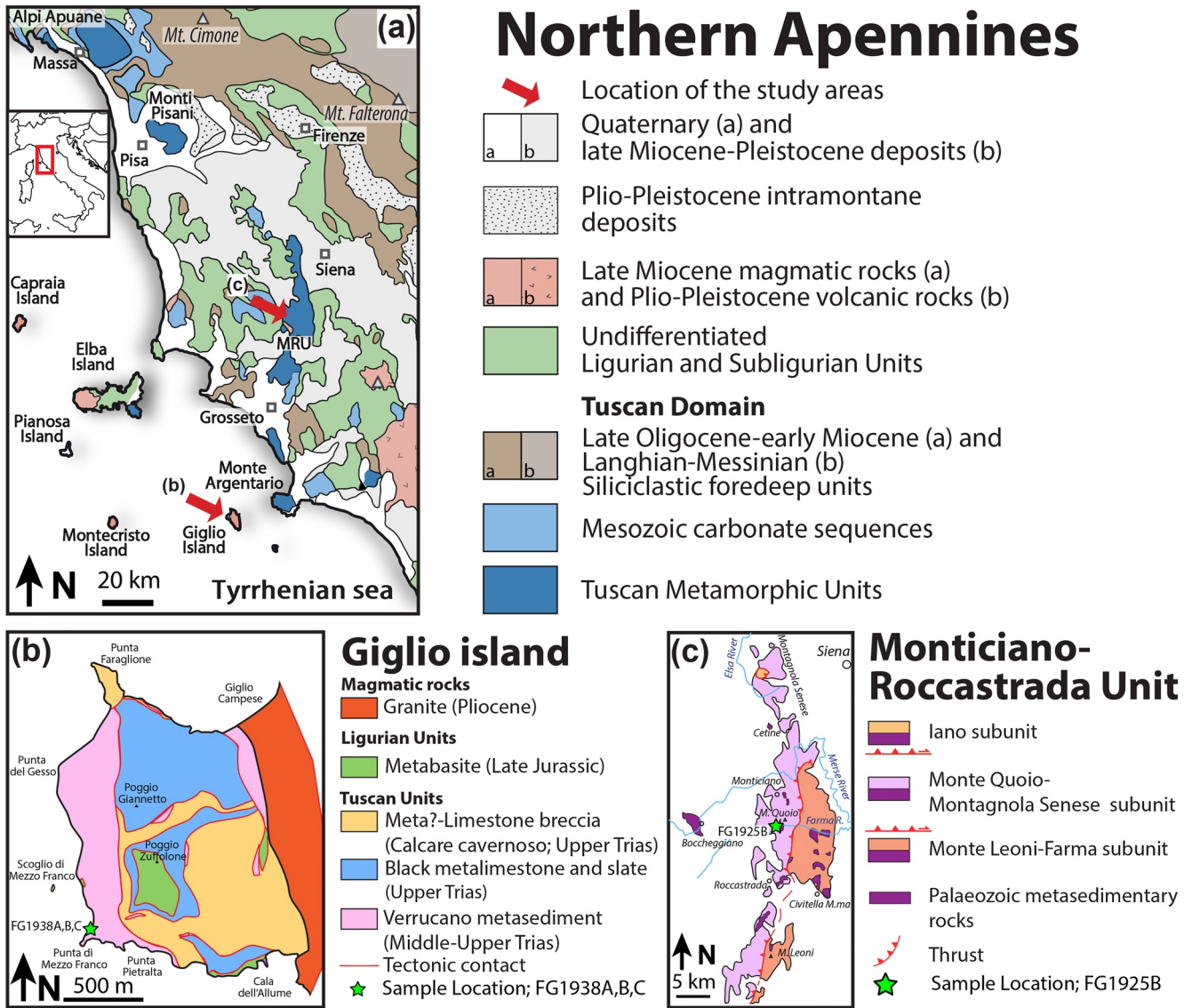


Figure 1. (a) Simplified geological setting of the Northern Apennines (based on Conti et al., 2020). MRU: Monticiano-Roccastrada Unit. (b) Tectonic map of the Franco Promontory in the Island of Giglio (based on Lazzarotto et al., 1964; Rossetti et al., 1999). (c) Tectonic map of the Monticiano-Roccastrada Unit with the location of the study area (after Brogi & Giorgetti, 2012; Lazzarotto et al., 2003).

2. Geological Setting

The Apennines are an orogenic belt developed from the Late Eocene as a result of the convergence between the European and African plates (Carminati & Doglioni, 2012; Molli, 2008; Vignaroli et al., 2009 and references therein; Figure 1a). The Northern Apennines comprise oceanic (Ligurian Metamorphic Units) and continental (Tuscan Metamorphic Units, TMU) units that experienced metamorphic conditions ranging from 0.8 to 1.6 GPa and 300–500°C between 27 and 18 Ma and subsequently were juxtaposed against non-metamorphic units (Bianco et al., 2019; Ryan et al., 2021 and references therein). In this study, we analyzed outcrops and samples from the Island of Giglio and the Monticiano-Roccastrada Unit located more than 80 km from one another along a transect oriented SW-NE, encompassing almost the entire width of the TMU (Figure 1).

2.1. Island of Giglio

The Island of Giglio (Tuscan Archipelago, Italy) is mostly made of a 5 Ma old monzogranitic intrusion (Peccerillo, 2005; Westerman et al., 1993). Tectonic slices of Ligurian Metamorphic Units and TMU crop out at the western side of the island as part of the pluton country rock (Franco Promontory; Lazzarotto et al., 1964; Rossetti et al., 1999, Figure 1b). The contact between the monzogranitic intrusion and the country rock is reworked by a top-to-the W high-angle normal fault. Metasedimentary sequences of the TMU comprise the Middle-Low Triassic clastic rocks of the Verrucano Formation (Azzaro et al., 1976) tectonically juxtaposed against a limestone unit of Upper Triassic age (Calcere Cavernoso Formation), metalimestone and slate (Lazzarotto et al., 1964; Rossetti et al., 1999).

The Ligurian Metamorphic Units and TMU on Giglio experienced polyphasic deformation and metamorphism (Jolivet et al., 1998; Lazzarotto et al., 1964; Rossetti et al., 1999), starting with a relic blueschist facies foliation preserved within a retrograde greenschist facies foliation. However, in the study area the Verrucano is predominantly associated with a blueschist facies mylonitic foliation and cut by veins that both formed at >1 GPa and 300–350°C, with only local and minor greenschist facies overprint (Giuntoli & Viola, 2022). In particular, pressure and temperature (P-T) conditions of vein formation were estimated by these authors on the same sample that has been studied in detail for microstructural analyses in this study (Sample A of Giuntoli & Viola, 2022 corresponding to FG1938A of this study).

2.2. Monticiano-Roccastrada Unit (MRU)

The MRU is composed of three thrusts with a N-S trend (Figure 1c; Costantini et al., 1988; Lazzarotto et al., 2003). Along the Farma River, the Palaeozoic-Triassic metasediments of the Arenarie di Poggio al Carpino Formation are deformed by a mesoscopic compressional duplex imbricates (Casini et al., 2007, 2008). The mylonitic foliation and veins associated with this structures formed at P-T conditions of >0.7 GPa and $\sim 400^\circ\text{C}$ and ~ 1.1 GPa and 350°C , respectively (Giuntoli & Viola, 2021). The FG1925 vein sample used for P-T estimates in Giuntoli and Viola (2021) has been investigated in detail for microstructural analyses in this study. Both duplex and thrust display kinematic indicators compatible with a top-to-the-E/NE sense of shear (Casini et al., 2007, 2008). Similar veins and metamorphic conditions were described also in surrounding areas of the MRU (Brogi & Giorgetti, 2012; Giorgetti et al., 1998).

3. Materials and Methods

Electron backscatter diffraction (EBSD) was performed on carbon-coated polished thin sections cut perpendicular to the foliation and parallel to the sample stretching lineation (Z and X in thin sections microphotographs and pole figures, respectively). EBSD patterns were collected using a 70° pre-tilted sample geometry, 20 kV accelerating voltage, a beam current of ~ 12.5 nA, 22.0 mm working distance, and 5 μm step size using a Hitachi VP-SEM with a Nordif UF-1000 EBSD detector (Chen et al., 2012). The Matlab toolbox MTEX (Bachmann et al., 2010, 2011; Mainprice et al., 2015) was used to process the data. Noise reduction was conducted to filter mis-indexed points and artifacts according to procedures described by Sørensen et al. (2020). High-angle grain boundaries were traced for a misorientation $>10^\circ$ whereas low-angle boundaries for misorientations in the 2– 10° interval. Before ODF calculations, quartz grains were merged along Dauphiné twin boundaries, with an acceptance angle of 15° between the misorientation and the ideal Dauphiné twin misorientation. Then merged grains below five pixels were filtered out of the data. ODF were calculated based on the cleaned EBSD data within the grains, that is, the ODF is weighted by the grain area, also describing the orientation spread within the grain. Point pole figures were also based on merged grains. Untwinned grains were plotted as one point per grain. For twinned grains the widest grain member of each merged grain was selected as host “seed,” as done for calcite by Ryan et al. (2021), and any merged grain member with misorientation less than 20° from the host seed were assigned as host and the rest were assigned as twins. The mean of the host orientations and the mean of the twin orientations were then extracted, as the average orientations of the Dauphiné twinned grains has no physical meaning. The extracted crystallographic directions were plotted on pole figures (lower hemisphere stereographic projection), all ODF were calculated from EBSD data in the merged grains using a de La Vallée Poussin kernel with halfwidth of 15° with J-index after Bunge (2013) and contouring as multiples of a uniform distribution (MUD). Misorientation angle distributions (MAD) were computed for correlated pairs (with a shared boundary)

and uncorrelated pairs and were correlated with the theoretical random distribution (e.g., Prior et al., 2002; Wheeler et al., 2001). EBSD grain size maps used the diameter of the grain equivalent circle. Grain orientation spread (GOS) maps display a measure of the internal strain of a grain defined as the average misorientation angle between each pixel in a grain and that grain's mean orientation (Wright et al., 2011). The kernel average misorientation (KAM) map displays a measure of the average misorientation around a measurement point with respect to a defined set of neighbor points.

Differential stress was computed by using the EBSD sliding resolution piezometer of Cross et al. (2017), which is based on the relationship $D = 10^{4.22 \pm 0.51} \cdot \sigma^{-1.59 \pm 0.26}$, where D is the root-mean-square value of mean diameter and σ is the flow stress. Strain rates were estimated using the dislocation flow law for quartz of Hirth et al. (2001).

The Mohr-Coulomb failure diagram (pore fluid factor (λ_v)-differential stress ($\sigma_1 - \sigma_3$)) was computed following Cox (2010) with the same parameters used by Menegon and Fagereng (2021), owing to the analogy of the studied lithotypes. In detail, a coefficient of internal friction (μ) of 0.75 was used for metaconglomerate-metarenite (Jaeger & Cook, 1979) and 0.3–0.5 for metapelite (Okamoto et al., 2019), a cohesive strength (C) of 20 and 5 MPa and a tensile strength (T) of 10 and 2.5 MPa for metaconglomerate-metarenite and metapelite, respectively (Sivakugan et al., 2014; Zhang et al., 2011). Diagrams were computed assuming a thrusting regime with the vertical stress σ_v corresponding to the minimum compressive stress σ_3 , and an optimally oriented fault (θ_{opt}) with the maximum compressive stress σ_1 . θ_{opt} is equal to $\frac{1}{2} \tan^{-1} \left(\frac{1}{\mu} \right)$.

Equations for extension failure and hybrid extensional failure are:

$$\lambda_v = \frac{\sigma_3 + T}{\sigma_v} \quad (1)$$

$$(\sigma_1 - \sigma_3) = \frac{2c}{\sin 2\theta_{opt}} \quad (2)$$

Equations for shear failure are

$$\lambda_v = \frac{[4C - \sigma_1 + 4\sigma_3]}{3\sigma_v} \quad \text{for } \mu = 0.75, \quad (3)$$

$$\text{or } \lambda_v = \frac{1}{2\sigma_v} \left[2C \tan \theta_{opt} - \left(\frac{1 - \cos 2\theta_{opt}}{\cos 2\theta_{opt}} \right) \sigma_1 + \left(\frac{1 + \cos 2\theta_{opt}}{\cos 2\theta_{opt}} \right) \sigma_3 \right] \quad \text{for different } \mu \quad (4)$$

Additionally, we assumed that extensional failure (Equation 1) only occurs for $(\sigma_1 - \sigma_3) < 4T$, and that hybrid extensional failure (Equation 2) occurs for $(\sigma_1 - \sigma_3) \leq 2.5C$ for $\mu = 0.75$ (Cox, 2010).

4. Results

Complementary mesostructural and microstructural data and description of the studied field sites and samples are detailed in Giuntoli and Viola (2021, 2022).

4.1. Mesostructural Analysis

4.1.1. Island of Giglio

Metasediments are composed of metapelite, metaquartzarenite, and metaconglomerate bands with thickness ranging from a few meters to several tens of meters. Weaker metapelites are the most abundant lithotype and include boudinaged layers of stronger metaconglomerate and metaquartzarenite forming a “broken formation” (*sensu* Festa et al., 2019; Giuntoli & Viola, 2022, Hsü, 1968; Figures 2 and 3). A metamorphic mylonitic foliation composed of muscovite, quartz, carpholite, rutile, and carbonate occurs parallel to the lithological boundaries resulting in a composite foliation (i.e., bedding + metamorphic foliation) dipping gently to the E (Stereoplots in Figure 4 of Giuntoli & Viola, 2022). A stretching lineation is present on foliation planes and is defined by quartz, carpholite, and muscovite grains and plunges gently to the W-SW (Figure 2a).

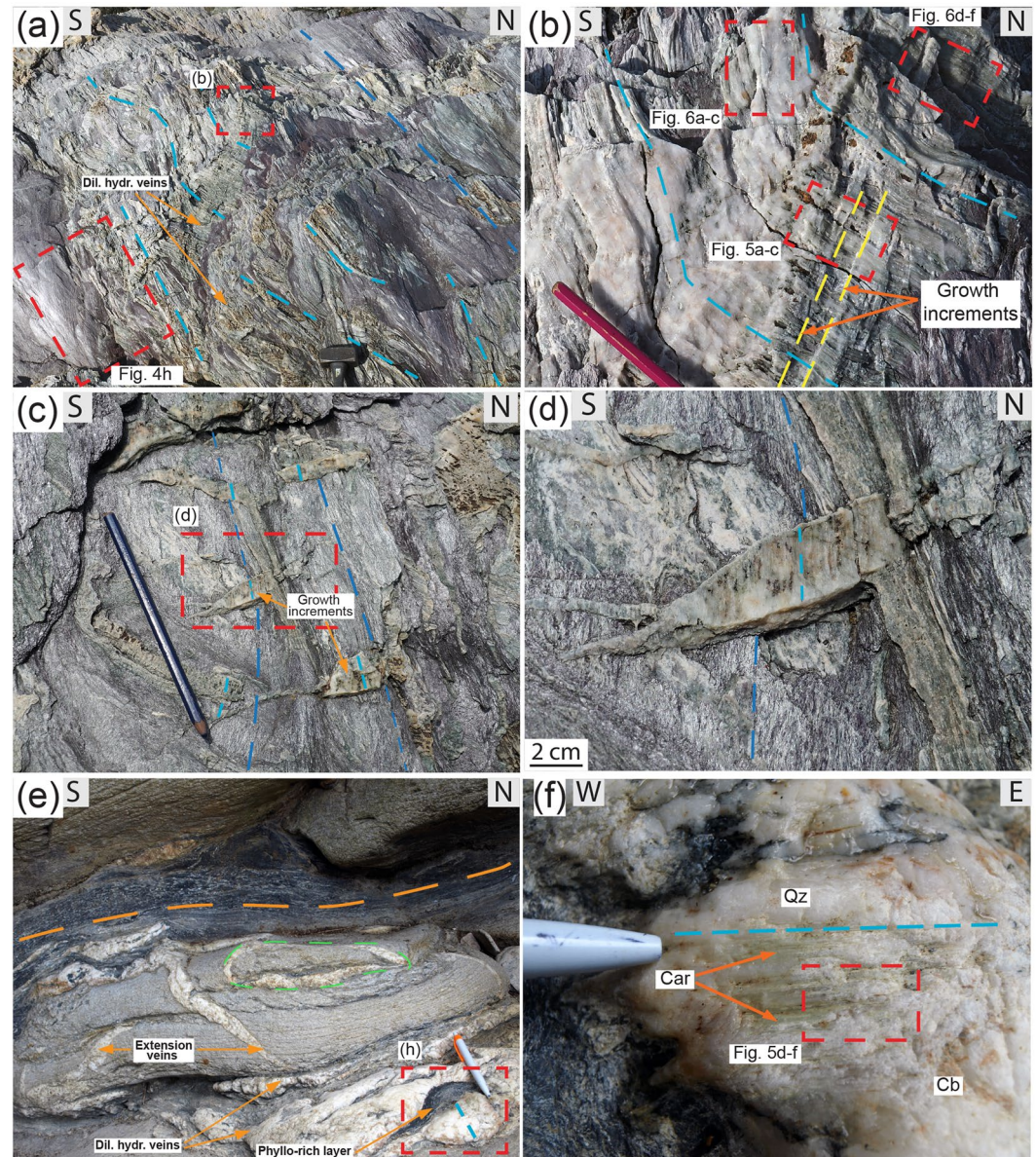


Figure 2. Metasediments and quartz and carpholite veins at the Island of Giglio (a–d) and Farma River (e and f). (a) Metapelite and quartz and carpholite dilational hydroshear veins. Dashed light blue and dark blue lines indicate fibers lengthening and stretching lineation in metapelite, respectively. (b) Detail of quartz and carpholite fibers (greenish-yellowish) of dilational hydroshear vein. Carbonate is locally intergrown with the previous minerals. Crack-and-seal growth increments are marked by fractures oriented parallel to the vein boundaries and highlighted by the dashed yellow line. The location of thin sections is marked. (c and d) Crack-and-seal growth increments cutting the stretching lineation in metapelite. (e) Bluish metapelite and greyish metaquartzarenite cut by dilational hydroshear and extensional veins. A non-cylindrical fold deforming a vein is highlighted by the green. The foliation trace is marked by the dashed orange. The direction of the stretching lineation is marked by the pen. (f) Detail of dilational hydroshear vein with quartz and carpholite fibers. The location of the thin section is marked. Mineral abbreviations in figures according to Whitney and Evans (2010). Orientation of photos: (a)–(d) and (f) parallel to the foliation plane, (e) perpendicular to foliation and stretching lineation). (a) Modified from Giuntoli and Viola (2022). (e and f) Modified from Giuntoli and Viola (2021).

Metapelites are schistous and characterized by a shiny violet to gray-green color (Figures 2a–2d). Metaquartzarenites and metaconglomerates are more massive and exhibit a white to light brown color (Figures 3a and 3b). The primary sedimentary texture is grain-supported, with rounded detrital quartz clasts from white to pink in color and a few hundreds of microns to some centimeters in size. The mylonitic foliation wraps around these clasts producing asymmetric pressure shadows composed of quartz, carpholite, and muscovite (Figure 3b).

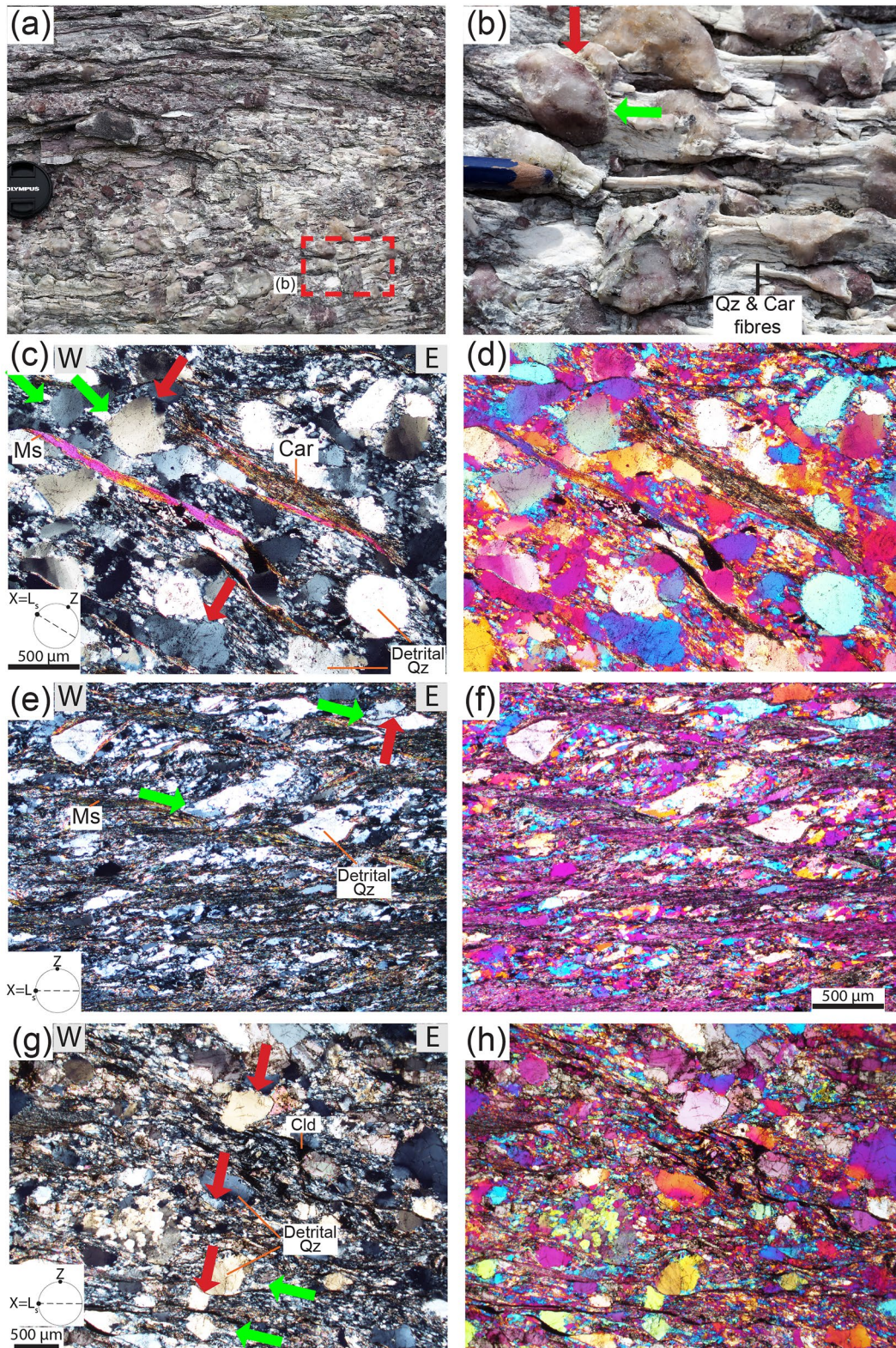


Figure 3.

Veins are very common in all lithotypes (Figures 2a–2d). They are both subparallel to the foliation and oriented at high angle to it. Veins sub parallel to the foliation mainly occur in metapelite, while those at high angle in metaquartzarenite and metaconglomerate. Vein geometry varies from straight to twined. In metapelite, veins are up to several meters long and a few decimeters thick and can represent a maximum of 50% of the rock volume. In metaconglomerate and metaquartzarenite, they are up to 1 m long, a few decimeters thick and can form up to ~10% of the entire volume of the rock. Both types of veins are cogenetic and thus broadly coeval, as shown by mutual crosscutting relations (see details in Giuntoli & Viola, 2022).

All veins are composed of quartz and carpholite fibers, some decimeters long. Fibers are cut across by thin sets of parallel fractures oriented perpendicularly to the fibers long dimension and to the foliation, representing growth increments by cracking-and-sealing (e.g., Cox & Etheridge, 1983; Durney & Ramsay, 1973, Figure 2b). Several generations of fibers are visible, from almost 1 m to a few millimeters in size (see details in the following sections for the microscale). Fibers are mainly iso-oriented parallel to the local stretching direction marked by the stretching lineation in the host rock, even though locally they display sharp changes in orientation on the foliation plane, especially where two adjacent crack-and-seal increments meet (Figure 2b). Additionally, in some areas, fibers separated by metapelite bands display different orientations, even if only a few centimeters away across the main foliation (Figures 4a–4c; see Section 5 for interpretation). Locally, quartz and carpholite fibers grow parallel to the axial surface of micrometer-scale crenulations in the metapelite (Figure 4b). Finally, some fibers are twined along their long axis (Figure 4d). Fibers plunge gently mainly to the E and secondarily to the N (Figure S5 of Giuntoli & Viola, 2022). The described structures display significant similarities with the “striped-bedding veins” of Koehn and Passchier (2000) and the “dilatational hydroshear veins” of Fagereng et al. (2010; see also Section 4.2 and Giuntoli & Viola, 2021, 2022 for additional details). In the following text, therefore, the term dilatational hydroshear vein will be used to describe veins subparallel to the foliation.

Commonly, non-cylindrical folds deform both veins and foliation. These folds do not affect the entire rock-volume but are restricted to bands from the meter to the micrometer scale leaving the surrounding bands or veins undeformed (Figures 4e–4g; see Section 4.2 for the microscale). The observed structures crop out over an area of ~1 km².

4.1.2. Farma River

Lithotypes cropping out at the Farma River share several similarities with the Island of Giglio. More competent metaquartzarenite and minor metaconglomerate bands form imbricated metric horses bounded by weaker metapelite bands, which form shear zones. The foliation is a composite foliation resulting from a metamorphic foliation overprinting the original bedding. The foliation is marked by muscovite, quartz, carpholite, chloritoid, rutile, and carbonate and dipping gently W-SW (stereonet in Figure 2 of Giuntoli & Viola, 2021). Metapelite displays a gray-bluish color and displays a mylonitic foliation with alternated phyllosilicate-rich bands and quartz-rich bands (Figure 2e). Metaquartzarenite shows a yellow-light gray color and displays original sedimentary grain size variations sub-parallel to the metamorphic foliation. Metaconglomerate occurs as discontinuous bands a few meters thick within metarenite, with mainly quartz and minor metapelite clasts. In all lithotypes quartz and phyllosilicates mark a stretching lineation that plunges gently W-SW.

As for the Island of Giglio, dilatational hydroshear veins occur in all lithotypes sub-parallel to the metamorphic foliation, but are more common in the metapelite, where they can be up to 1 m long and up to a few dm thick (Figures 2e and 2f). Extension veins are oriented at high angle to the foliation in the metaquartzarenite. Dilatational hydroshear veins and extension veins display no consistent crosscutting relations, indicating that those are coeval and genetically associated (more details in Giuntoli & Viola, 2021). At the Farma River, veins are volumetrically less abundant and form ~1–2 vol% of the entire outcrop. Veins are formed by quartz and carpholite

Figure 3. Blueschist facies foliation in metaconglomerate and metaquartzarenite. (a) Metaconglomerate with rounded quartz clasts from pink to white in color. (b) Enlargement showing quartz and carpholite fibers located in the asymmetric strain shadows of the clasts. Several clasts are interpenetrated at sites of high normal stress (red arrow) and asymmetric pressure shadows occur at sites of low normal stress (green arrow). (c–h) Thin section photos of metaquartzarenite with quartz detrital clasts. (c and d) The clasts are wrapped by the blueschist facies foliation producing asymmetric pressure shadows marked by carpholite and white mica. Monomineralic quartz bands are composed of equant grains and a few core-and-mantle structures are present. (e and f) Metaquartzarenite displays detrital quartz clasts overgrown epitaxially in the asymmetric strain shadows. The white mica marks top-to-the-E extensional crenulation cleavage. (g and h) Metaquartzarenite with quartz clasts wrapped by chloritoid oriented both perpendicular and parallel to the foliation. Crossed-polarized light (c, e, g) and crossed-polarized light with gypsum plate inserted (d, f, h). Island of Giglio (a–f) and Farma River (g and h). Orientation of photos: all pictures are oriented perpendicular to foliation (Z), parallel to the pole of the foliation, and parallel to the stretching lineation ($X = L_s$). Insets (e and f) modified from Giuntoli and Viola (2022).

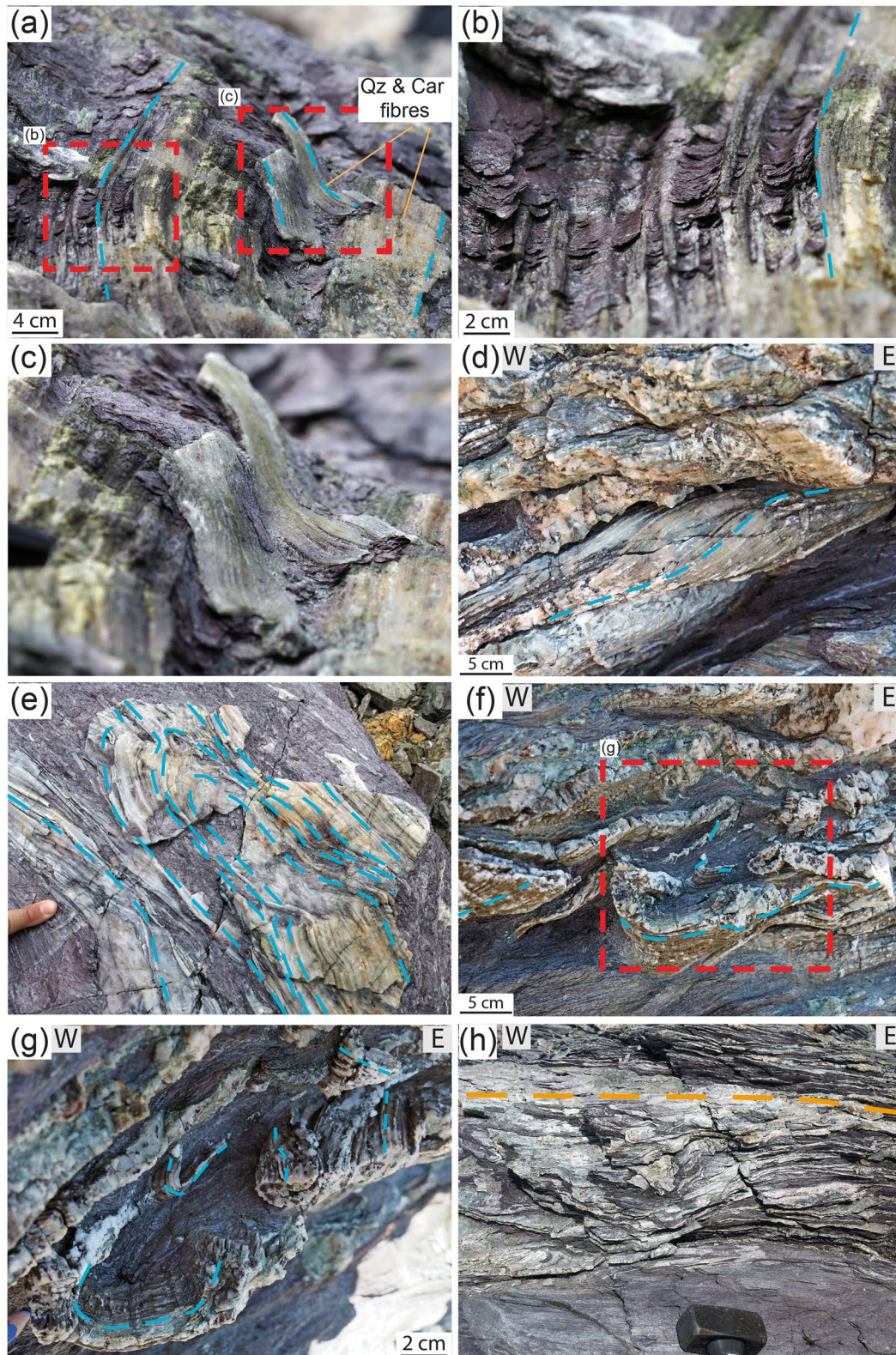


Figure 4.

fibers describing a stretching lineation with the same orientation as the one in the host rock (Figure 2f). Locally, isoclinal non-coaxial folds lengthened parallel to the direction of stretching deform some veins (green dashed line in Figure 2e).

4.2. Petro- and Microtectonics

Owing to the mineralogical and microstructural similarities between the two study areas, sample description is done together in this text. The metapelite displays a foliation defined by the grain shape preferred orientation of white mica, quartz, rutile, and carbonate, with carpholite only present in samples from the Island of Giglio and pyrophyllite and chloritoid in samples from the Farma River (see phyllosilicate-rich layers in Figures 5–7). Metaquartzarenites and metaconglomerates contain rounded and a few angular quartz clasts with undulose extinction wrapped by a foliation marked by muscovite, quartz, carpholite, chloritoid (only at Farma River), rutile, and carbonate. Quartz clasts are commonly interpenetrated at sites of high normal stress and asymmetric pressure shadows occur at sites of low normal stress (red and green arrows in Figures 3c–3h, respectively). Phyllosilicates are generally found between interpenetrated grains. The asymmetric pressure shadows are marked by muscovite, carpholite and chloritoid (the latter is present only at the Farma River) and quartz marking the stretching lineation on foliation planes. In the pressure shadows, quartz is finer grained and overgrows epitactically the clasts (Figures 3c–3h). These microstructures are indicative of dissolution-precipitation creep (e.g., Bell et al., 1986; Hippertt, 1994; Menegon, Pennacchioni, & Spiess, 2008; Stöckhert et al., 1999; Trepmann & Seybold, 2019; Wintsch & Yi, 2002). Monomineralic quartz bands are composed of equant grains and a few core-and-manle structures are visible, with the larger grains showing lobate grain boundaries and undulose extinction, thus suggesting a contribution of dislocation creep and subgrain rotation recrystallization (Figures 3c–3h; e.g., Lloyd & Freeman, 1994; Nishikawa et al., 2004; Stipp et al., 2002a; Trimby et al., 1998; Urai et al., 1986).

Dilational hydroshear veins contain quartz and carpholite-rich bands and muscovite-rich bands (Figures 5–7). Carbonate occurs locally within bands oriented parallel to the fibers and along fractures cutting through them. Quartz and carpholite fibers are interfingered and iso-oriented and display a marked shape preferred orientation parallel to the foliation (Figure 5). Along discrete bands, quartz fibers display undulose extinction and are composed of smaller equant grains (see details in the next section). Locally, quartz bands display pinch and swell structures, boudins and incremental crack-and-sealing stages (Figure 5 and Figure 6, see details in the following section). Carpholite fibers are also boudinaged and finer-grained carpholite and quartz occur in the boudin necks (Map 7 in Figures 5a–5c). Frequently, carpholite displays a murky aspect in optical plane-polarized light due to incipient retrogression.

Quartz fibers contain abundant fluid inclusion bands oriented perpendicular to the lengthening of the fibers and to vein boundaries. These inclusion bands display a spacing of a few tens of microns (e.g., Figures 8a–8c; more details in the following section). These inclusions contain liquid + vapor phases (Rossetti et al., 1999). This microstructure was interpreted as healed microcracks related to incremental crack-and-seal growth steps (e.g., Bons et al., 2012; Condit & French, 2022; Cox & Etheridge, 1983; Durney & Ramsay, 1973; Fisher & Brantley, 1992; Koehn & Passchier, 2000; Raimbourg et al., 2021; Ramsay, 1980; Trepmann & Seybold, 2019). The same mechanism is also described for dilational hydroshear vein (Fagereng et al., 2011; Giuntoli & Viola, 2021, 2022; Ujiie et al., 2018).

Muscovite and pyrophyllite (the latter only present at the Farma River) bands occur within the veins oriented parallel to the lengthening of the fibers and with a thickness of a few mm (Figure 5). These bands appear dark at the optical microscope with plane polarized light due to inclusions of graphite, rutile (and, additionally, hematite and pyrite at Giglio and Farma, respectively) a few microns in size. These phyllosilicate bands are interpreted as remnant of previous foliation planes exploited by the dilational hydroshear veins (Bons et al., 2012; Cox & Etheridge, 1983; Fagereng et al., 2011; Fisher & Brantley, 1992; Giuntoli & Viola, 2021; Koehn & Passchier, 2000; Ramsay, 1980; Trepmann & Seybold, 2019). Importantly, these phyllosilicate bands can potentially act as slip planes thus allowing localized shearing and displacement accumulation inside the veins, as

Figure 4. Quartz and carpholite dilational hydroshear veins in metapelite from the Island of Giglio. Dashed light blue and blue lines indicate fibers lengthening. (a and b) Fibers growing parallel to the axial surface of crenulations in metapelite and fibers separated by metapelite bands displaying different orientation. (c) Detail of (b). (d) Locally, fibers are twined along their long axis. (e–g) Non-cylindrical folds deforming dilational hydroshear veins. (f and g) Folds confined to some bands deforming fibers with different orientations a few centimeters away. (h) Detail of Figure 2a showing long dilational hydroshear veins in metapelite (dashed orange line: foliation trace). Inset (e) modified from Giuntoli and Viola (2022).

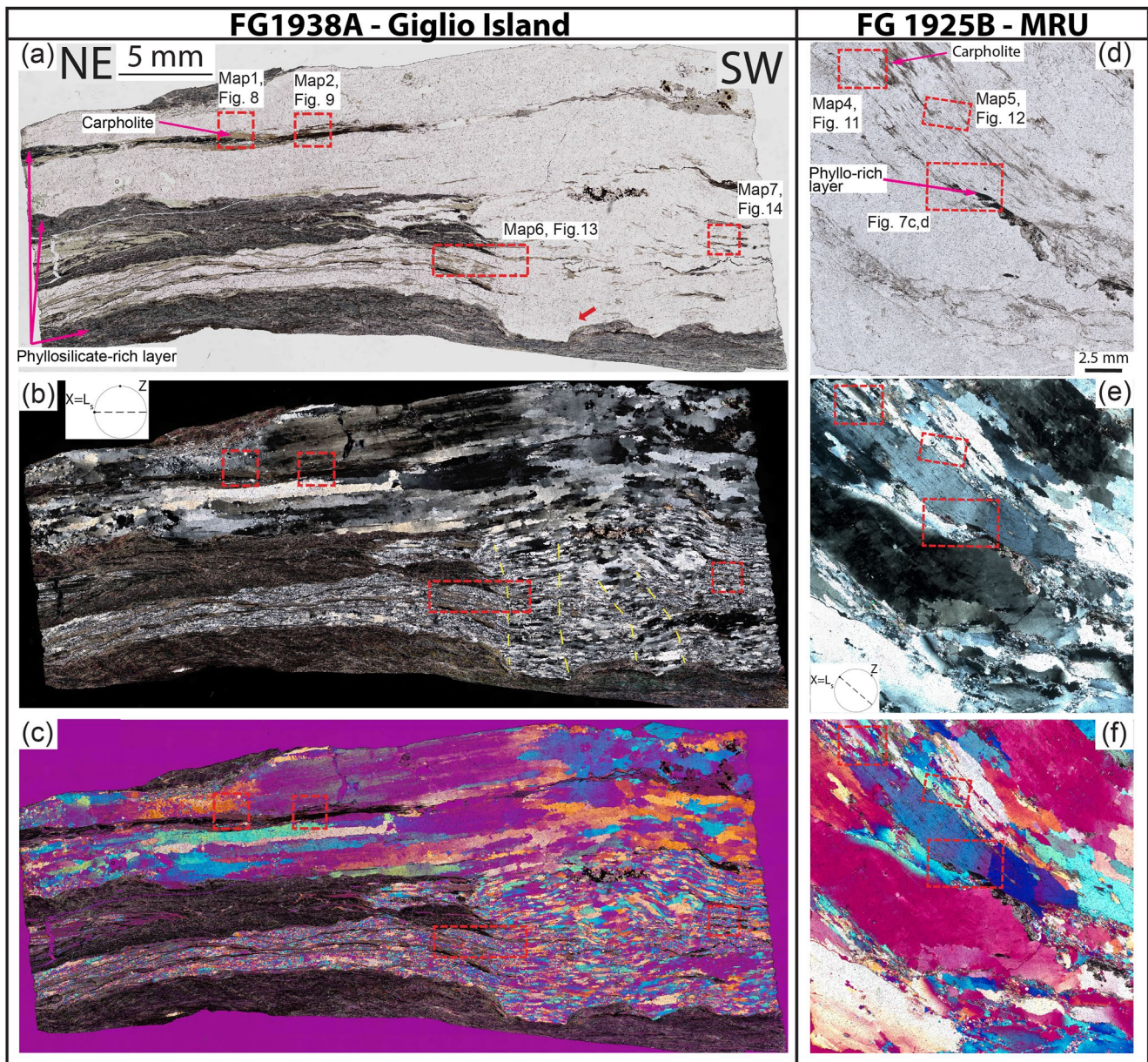


Figure 5. Thin section scans of dilational hydroshear veins at the Island of Giglio (a–c, sample FG1938A) and Farma River (d–f, FG1925B). Quartz bands display fibers some centimeters in length with undulose extinction and more deformed fibers with smaller grain size (see text). Mica-rich bands appear dark due to micron-sized inclusions of graphite, rutile, hematite (at Giglio) and pyrite (at Farma). Carpholite fibers display colorless to brownish (incipient retrogression) absorption colors. Incipient boudinage is visible in sample FG1938A between stronger quartz bands and weaker muscovite bands (red arrow), as well as stretched fibers related to incremental crack-and-seal (dashed yellow lines). Plane-polarized light (a and d). Crossed-polarized light (b and e) and crossed-polarized light with gypsum plate inserted (c and f).

described (albeit for shallower conditions) by other authors (Figures 7a–7d; “transform fault” in Figure 7 of Labaume et al., 1991; “microfault” in Figure 18 of De Roo & Weber, 1992; “inclusion trail” in Figure 6 of Koehn & Passchier, 2000; “micro-transform” in Figure 3 of Fagereng et al., 2010).

Locally, phyllosilicate bands define rootless folds and dilational hydroshear veins are deformed by isoclinal non-coaxial folds (Figures 6d–6f and 7e–7h). Commonly, folding affects only some bands, leaving adjacent fibers almost undeformed (red arrow in Figure 6f and top part of thin section scan visible in Figures 6d–6f and 7e–7f, see also Section 5.1 for interpretation). Summarizing, field and microscopic observations show that the analyzed

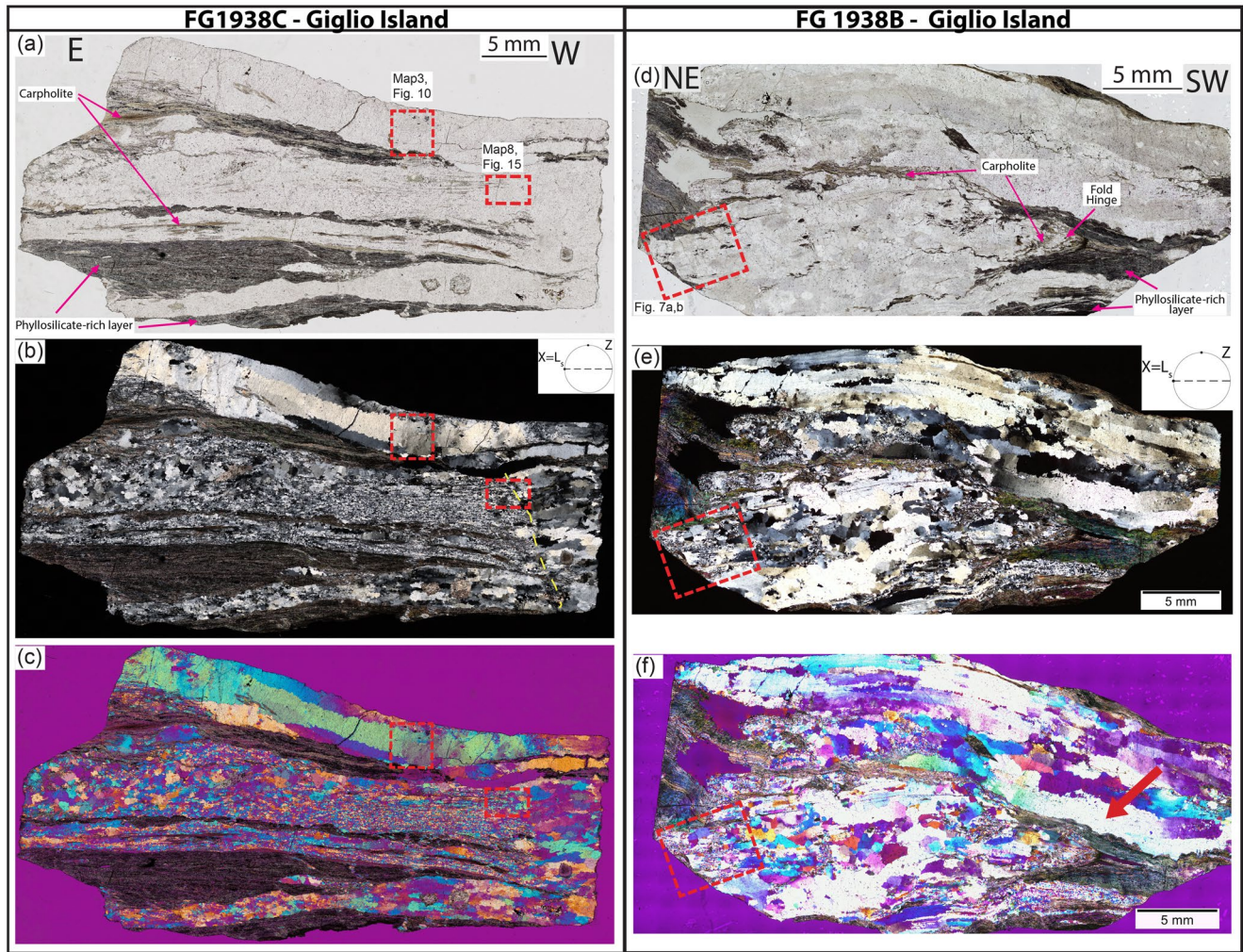


Figure 6. Thin section scans of dilational hydroshear veins at the Island of Giglio. (a–c) In sample FG1938C quartz-rich bands are composed of either fibers some centimeters long with undulose extinction (top part) or equant grains with smaller grain size (center and bottom). These bands are bounded by mica and carpholite rich bands. Discrete quartz stretched fibers related to incremental crack-and-seal is located to the right (dashed yellow line). (d–f) Sample FG1938B shows quartz fibers some centimeters long with undulose extinction (red arrow and top part of the thin section) and isoclinal fold surrounded by muscovite and carpholite (bottom). Plane-polarized light (a and d). Crossed-polarized light (b and e) and crossed-polarized light with gypsum plate inserted (c and f).

samples display mutual overprinting relationships between brittle and ductile structures (see additional supporting evidence in Giuntoli & Viola, 2021, 2022).

4.3. EBSD Analysis

We acquired eight EBSD maps on quartz from dilational hydroshear veins from the Island of Giglio (samples FG1938A and C; Figures 5a–5c and Figures 6a–6c, respectively) and from the MRU (sample FG1925B; Figures 5d–5f). Note that samples FG1938A and FG1925b were used to constrain P-T conditions of vein formation in Giuntoli and Viola (2021, 2022). Carpholite in the maps could not be indexed, possibly due to partial retrogression of the grains or polishing-induced damages. Our EBSD maps cover representative areas from three different microstructural domains, which are discussed in detail below: (i) centimetre-long quartz fibers, (ii) recrystallized quartz ribbons at the edge of quartz fibers, and (iii) quartz, carpholite, and muscovite layers.

1. Centimetre-long quartz fibers are mainly oriented parallel to the stretching lineation of the host rock visible in the field. Quartz fibers display a strong shape preferred orientation (SPO), are characterized by high aspect ratios (up to 30) and display undulose extinction, with grain size reduction at their edges. These fibers do not

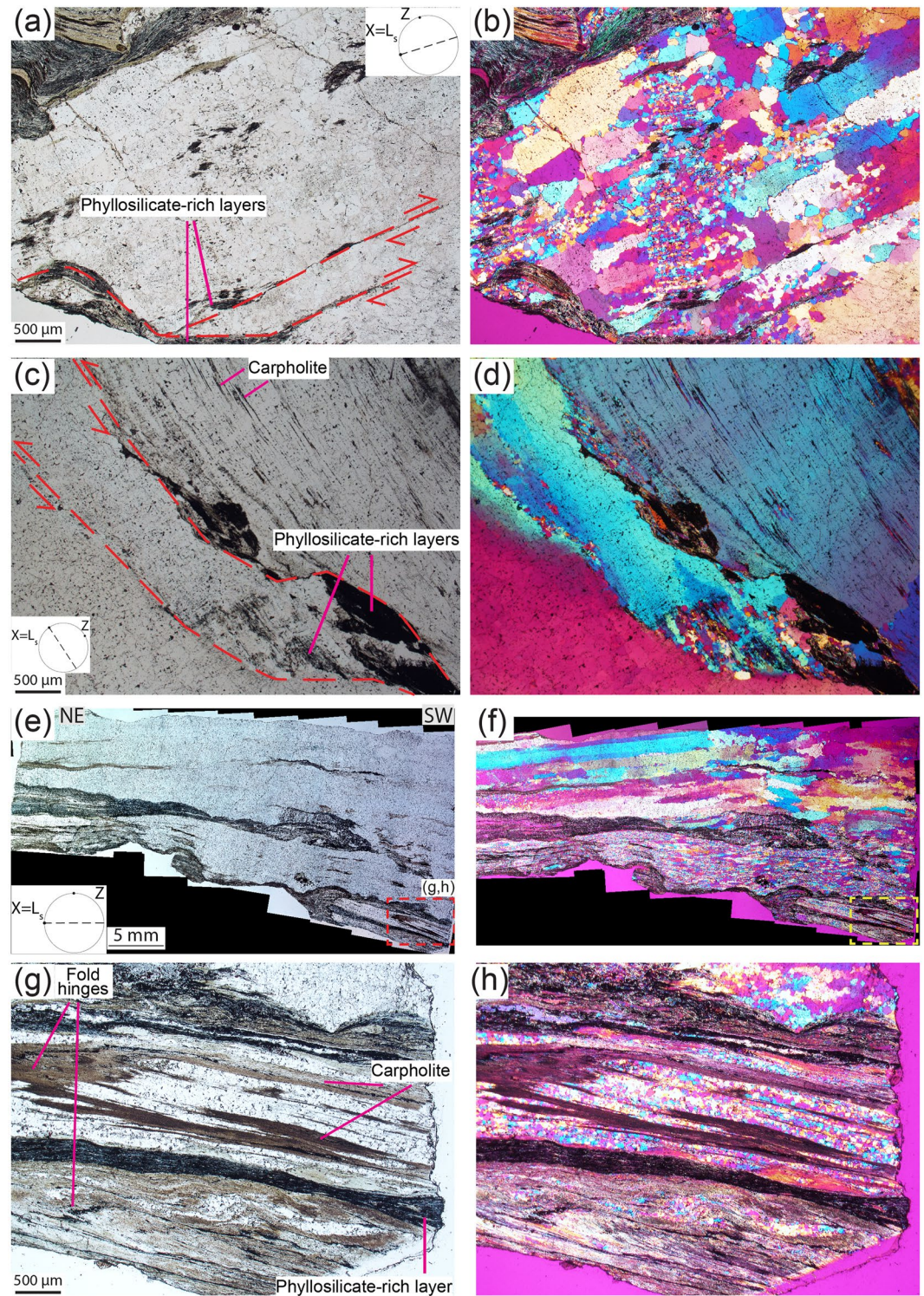


Figure 7. Examples of textural relationships between quartz and phyllosilicate-rich layers. Thin section photos and scans of dilational hydroshear veins from the Island of Giglio (a and b sample FG1938B and e–g representing a second thin section from sample FG1938A) and Farma River (c and d, FG1925B). (a–d) Thin, discrete phyllosilicate-rich layers separating contiguous quartz fibers (dashed red lines). The sense of shear is marked by the red arrows. See locations in Figures 5d and 6d. (e–h) Isoclinal non-coaxial folds with folded carpholite and muscovite in the hinges, carpholite oriented parallel to the axial plane, and polygonized equant or slightly elongated quartz grains. Quartz fibers located in the top portion of the thin sections are up to some centimeters long with undulose extinction.

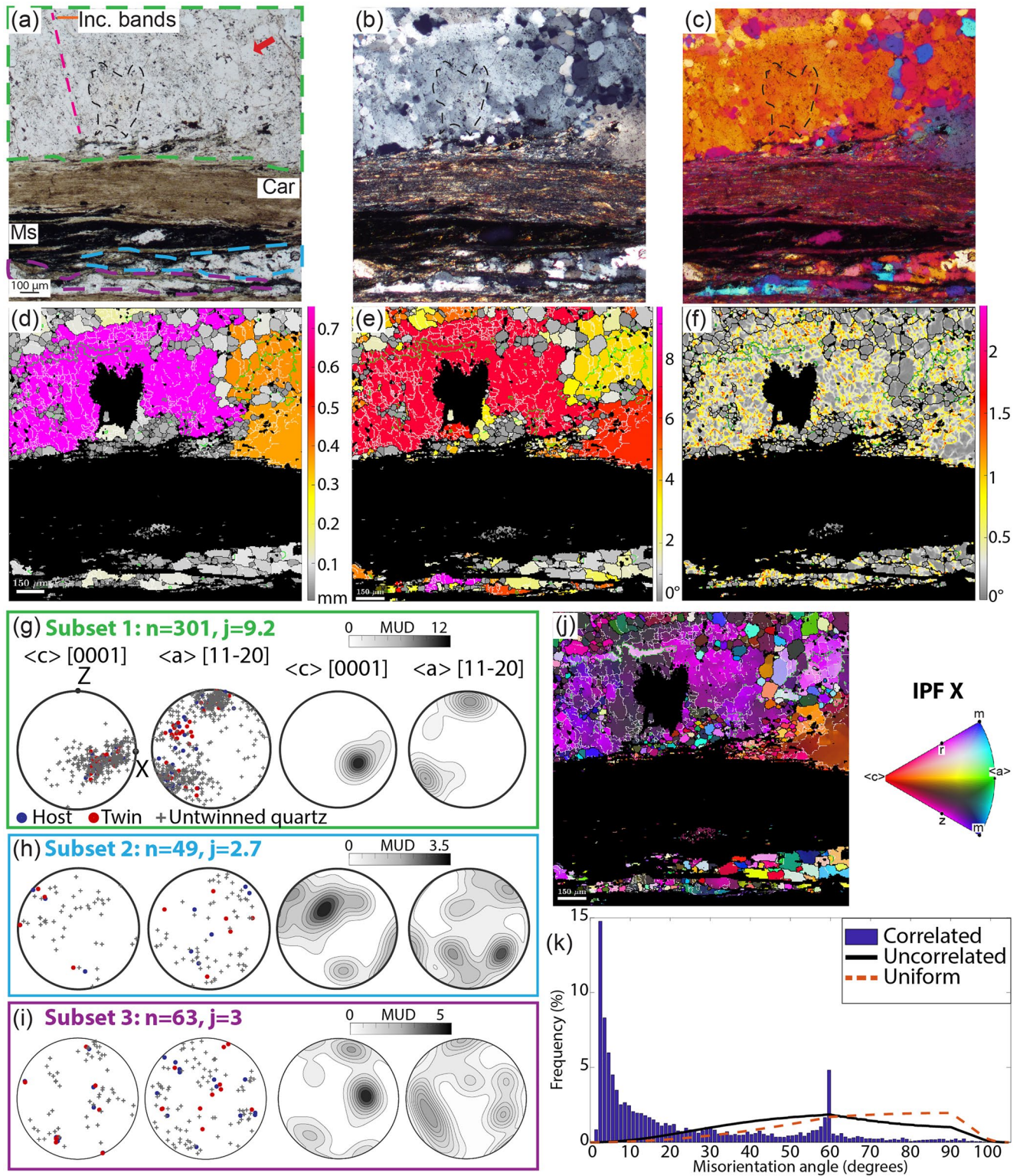


Figure 8.

- share a common crystallographic preferred orientation (CPO), as visible in the optical thin section scans with crossed-polarized light and the gypsum plate inserted (Figures 5c, 5d, and 6d).
2. Recrystallized quartz ribbons commonly represent the lateral termination of quartz fibers and are composed of polygonized equant smaller grains ($<100\ \mu\text{m}$; see next section for details) with low aspect ratios (<3). These ribbons are bounded laterally and vertically by phyllosilicate and carpholite grains.
 3. Quartz, carpholite, and muscovite layers are oriented parallel to the main foliation of the host rock. Quartz is interfingering with carpholite and exhibits generally polygonal equant grains, with a few larger grains displaying higher aspect ratios and SPO parallel to the foliation.

These three categories represent endmember cases, with intermediate cases also visible in thin section. In the following, we will characterize the microstructures of these domains as constrained by EBSD analysis.

4.3.1. Centimetre-Long Quartz Fibers

Maps 1 and 2 from sample FG1938A were acquired on one single, laterally continuous quartz fiber exhibiting incipient grain size reduction at the edges (subset 1 in map 1 and 1 and 3 in map 2 in Figures 8 and 9, respectively and Figure S1 in Supporting Information S1). The fiber is sandwiched between rather murky carpholite and muscovite grains due to abundant, micrometer-sized inclusions of hematite, graphite, and rutile (chemical analyses in Giuntoli & Viola, 2022). Carpholite and muscovite grains define areas with smaller quartz grains (subsets 2 and 3 in map 1, and 2 in map 2, Figures 8 and 9). Map 3 from sample FG1938C was acquired where a centimetre-long fiber is bent (subset 1) and subgrains are present, with discrete recrystallized domains composed of smaller equant grains (subsets 2 and 3; Figures 6a–6c and 10).

In all these maps, quartz fibers contain abundant fluid inclusion bands spaced at a few tens of microns, except where recrystallization occurs. There, polygonal equant grains are devoid of or contain only few fluid inclusions and appear bright in the optical pictures with plane-polarized light (arrow in Figure 8a). In the grain size maps, the coarse quartz grains display lobate high-angle grain boundaries (misorientation $>10^\circ$) and contain several low-angle boundaries (misorientations between 2° and 10°) defining numerous subgrains (black and white lines, respectively, in Figures 8, 9 and 10d). The small subgrains have a grain size similar to the equant grains along the boundaries of coarser grains. Quartz grain size varies between >1 and $2\ \text{mm}$ (map 1 and 3, respectively), as the coarsest quartz grains extend outside the map and a few tens of microns. Grain orientation spread (GOS) maps display generally higher values up to $8\text{--}10^\circ$ for larger grains and values $<2^\circ$ for grains smaller than $200\ \mu\text{m}$. A few exceptions occur, such as small grains containing abundant subgrains and exhibiting GOS values up to 8° (subset 3 of map 1 in Figure 8e) and the biggest grain of map 2 with GOS value of 4° (Figure 10e).

Kernel average misorientation (KAM) maps highlight two sets of misorientations characterized by values up to 1.5° (Figures 8f, 9f and 10f). The main set is oriented at high angle to the fiber lengthening direction (i.e., perpendicular to the foliation) and cuts across several grains. The second set of misorientations is oriented at almost 90° and is parallel to the fibers. The main set matches with subgrains boundaries and fluid inclusion bands as seen in the optical photos, the second set corresponds only to subgrains boundaries. As described above, equant smaller grains are generally devoid of or display scarce misorientation boundaries and appear bright in plane-polarized light photos.

Pole figures and the orientation distribution function (ODF) of quartz fibers and recrystallized grains show a well-defined CPO with the c-axes defining a strong maximum centered around X (subset 1 of map 2 in Figure 9g), forming an incomplete girdles in the XY plane (subset 1 of map 1 in Figure 8g), at high angle to X and Z (in subset 3 of map 2, Figure 9i), or displaying a strong maximum at small angle to Z and a minor maximum

Figure 8. Electron backscatter diffraction (EBSD) map 1 investigating the lateral termination of a centimetre-long quartz fiber (subset 1, highlighted by green dashed line in the present and following figures) bounded by carpholite and muscovite grains surrounding smaller quartz bands (subsets 2 and 3, light blue and purple dashed lines, respectively, in the present and following figures). The black dashed line marks quartz unindexed in the maps. The magenta dashed line highlights a fluid inclusion band, the red arrow indicates a polygonized equant grain devoid of fluid inclusions. (a) Plane-polarized light, (b) crossed-polarized light, and (c) crossed-polarized light with gypsum plate inserted. (d) Quartz grain size map. In this and following figures white lines indicate low-angle boundaries ($2^\circ\text{--}10^\circ$), black lines high-angle boundaries ($>10^\circ$), and light blue lines Dauphiné twin boundaries in quartz. (e) Quartz grain orientation spread (GOS) map. (f) Quartz kernel average misorientation (KAM) map displays a dense set of misorientations that matches with fluid inclusion band visible in the optical photos and with subgrains boundaries. Note that recrystallized grains are devoid of misorientation boundaries (see text). (g–i) Quartz pole figures of crystallographic axes for the subsets defined in (a). Pole figures are plotted on the lower hemisphere of the stereographic projection. n = number of grains (one point per grain). Half width 15° and cluster size 5° , maximum value and J-index are given. (j) IPF map color-coded with respect to the X-kinematic direction. (k) Misorientation angle distributions (MAD) of quartz grains displaying peaks at low angle misorientations and at 60° for correlated pairs.

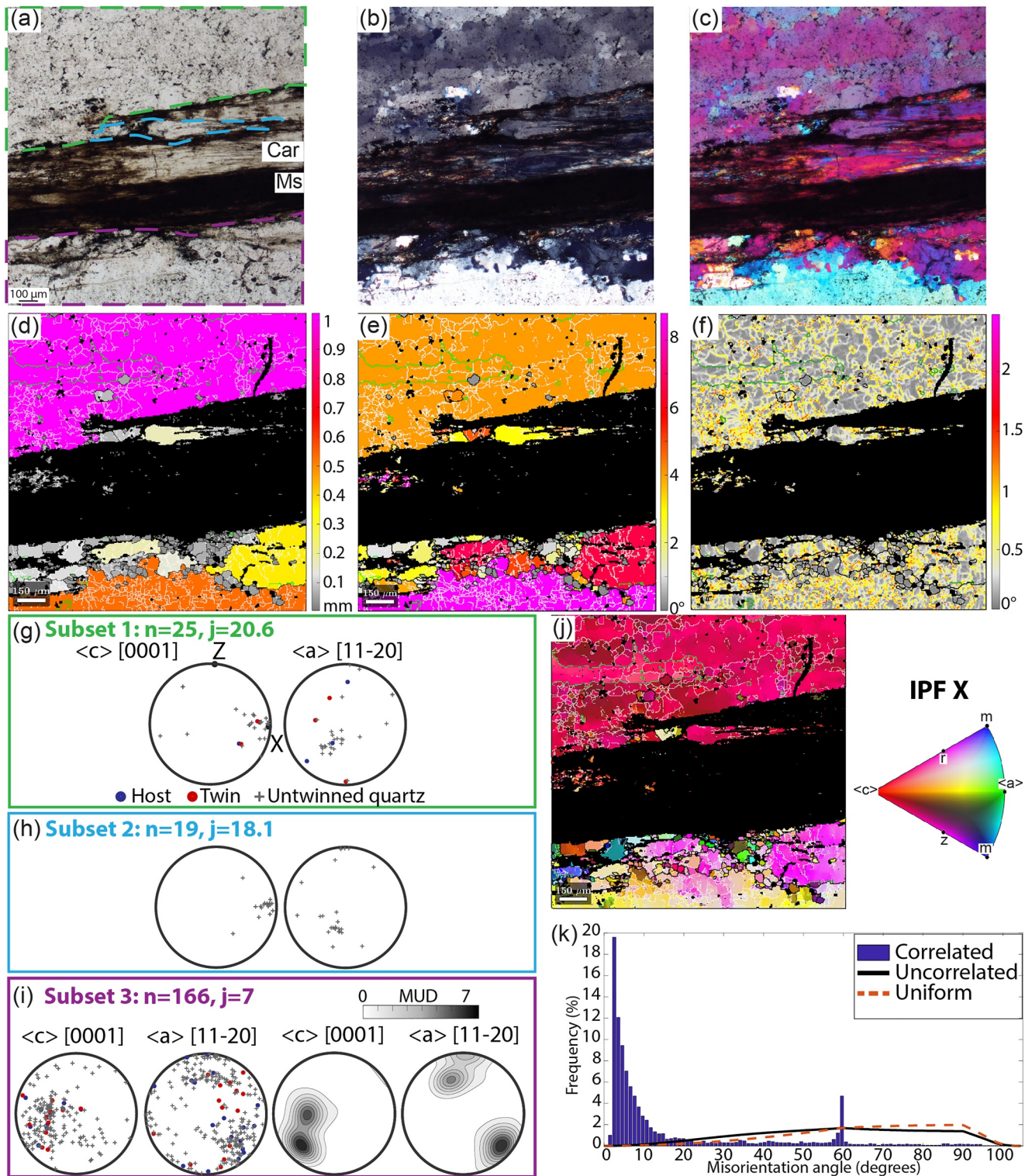


Figure 9. Electron backscatter diffraction (EBSD) map 2 investigating the lateral continuation of the quartz fiber visible in map 1 (subset 1), quartz grains surrounded by carpholite and muscovite bands (subset 2), and another quartz fiber (subset 3). Compare with chemical map of this site in Giuntoli and Viola (2022). (a) Plane-polarized light, (b) crossed-polarized light, and (c) crossed-polarized light with gypsum plate inserted. (d) Quartz grain size map. (e) Quartz grain orientation spread (GOS) map. (f) Quartz kernel average misorientation (KAM) map. (g–i) Quartz pole figures (j) IPF map. (k) Misorientation angle distributions (MAD) of quartz grains.

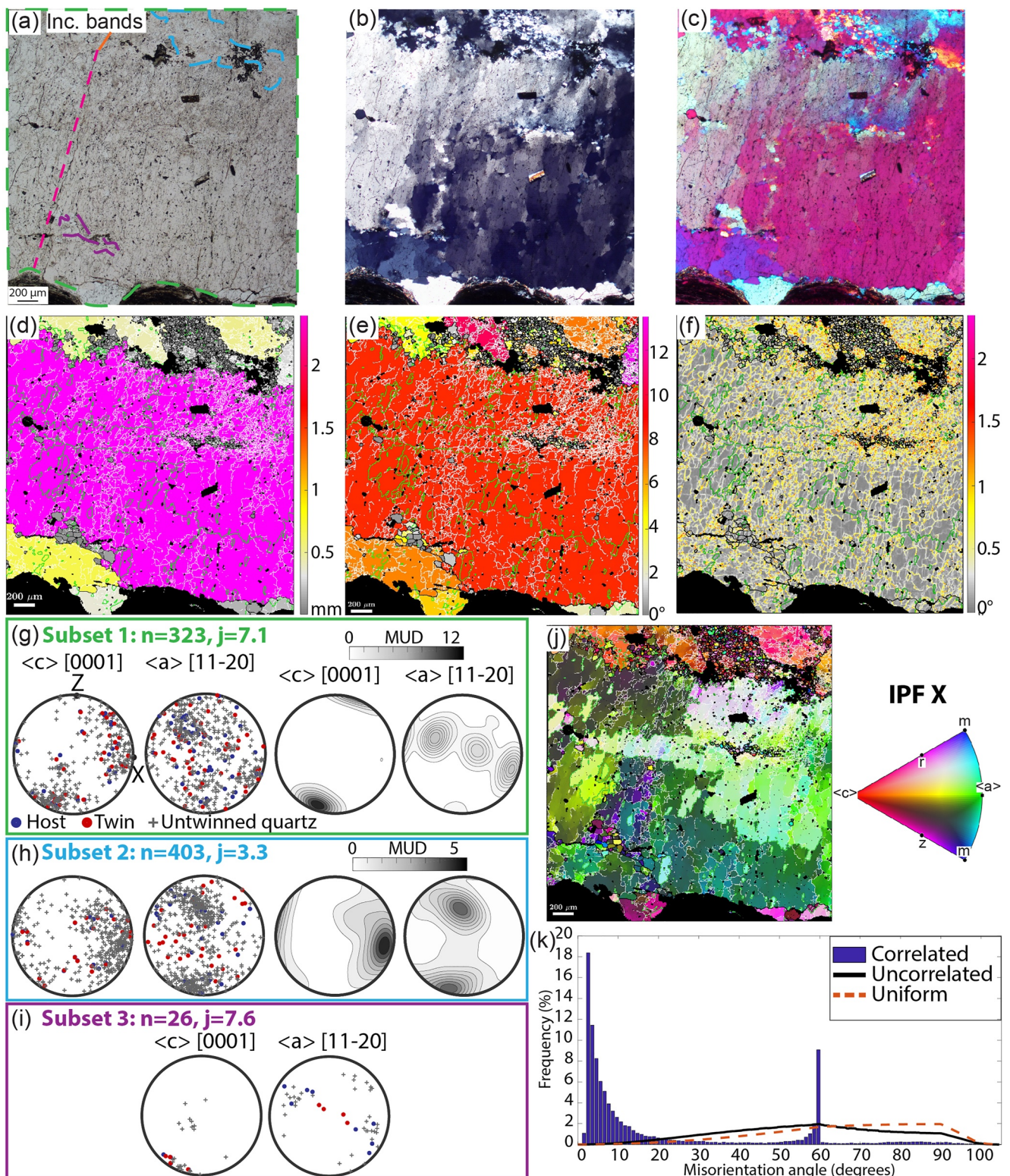


Figure 10. Electron backscatter diffraction (EBSD) map 3 acquired where a centimetre-long fiber of quartz is bent (subset 1) and subgrains are forming (subsets 2 and 3). (a) Plane-polarized light, (b) crossed-polarized light, and (c) crossed-polarized light with gypsum plate inserted. (d) Quartz grain size map. (e) Quartz grain orientation spread (GOS) map. (f) Quartz kernel average misorientation (KAM) map. (g–i) Quartz pole figures. (j) IPF map. (k) Misorientation angle distributions (MAD) of quartz grains.

coinciding with X (subset 1 of map 3 in Figure 10g). J-indexes vary between 7 and 20.6, probably owing to inheritance from one or a few large grain orientation(s). Quartz grains located between bands of carpholite and muscovite are characterized by a weaker CPO for the c-axis, with girdles on the XZ planes (subsets 2 and 3 of map 1, with J-index of 2.7 and 3, respectively in Figures 8h and 8i), except in map 2, where subset 2 shows a strong maximum around X, similarly to subset 1 from the same map (Figures 9g and 9h). The recrystallized domains of the quartz fibers either contain a weak CPO with the c-axis along the XZ plane (subset 2 of map 3, Figure 10h) or a strong CPO with a c-axis maximum at small angle to Z (subset 3 of map 3, Figure 10i), similarly to subset 1 from the same map.

The presented inverse pole figure maps were color-coded with respect to the X-kinematic axis (IPF). They show that smaller equant grains adjacent to the bigger fibers share a similar crystallographic orientation (i.e., they are characterized by similar colors; Figures 8j, 9j and 10j). The misorientation angle distribution (MAD) of correlated pairs of grains shows peaks between 2° and 10° . This distribution is compatible with the effects of subgrain rotation recrystallization occurring via formation of high-angle boundaries resulting from continuous rotation of subgrains (Neumann, 2000, Figures 8k and 9k and Figure 10k). The peak around 60° is associated with Dauphiné twinning (Lloyd, 2004; Menegon et al., 2011). The uncorrelated grains distribution is similar to the theoretical (uniform) distribution.

As described in Section 4.1.2, sample FG1925B is from an outcrop with a subhorizontal stretching lineation. Thin section scans and maps were acquired with the stretching lineation oriented at almost 45° to the horizontal (Figures 11 and 12). Maps 4 and 5 display acicular crystals of carpholite included within or interfingering with quartz fibers. Quartz subgrains and smaller equant grains form preferentially at the edge of quartz fibers (subsets 1 of map 4 and 1–3 of map 5; Figures 11 and 12) or forming discrete recrystallized domains (subset 2 of map 4, Figure 11). As in the other described samples, the bigger fibers are prismatic, have high aspect ratios (up to 10) and are up to 1.4 mm long in the maps and 10 mm long in the thin section (Figures 11 and 12d). The smaller recrystallized grains are either equant or display low aspect ratios and have a grain size $<200 \mu\text{m}$. In the fibers, the smaller subgrains and Dauphiné twins display a size $<200 \mu\text{m}$, similar to the equant grains. In map 5 some Dauphiné twins are stretched parallel to the lengthening of the quartz fibers and show a continuity to carpholite acicular grains included in the quartz fiber (arrow in Figure 12d).

GOS maps display values up to 8° – 10° for bigger grains containing numerous subgrains and Dauphiné twinning boundaries, and values lower than 2° for grains below $200 \mu\text{m}$ (Figures 11e and 12e). Noteworthy, a few exceptions are present, with grains $<200 \mu\text{m}$ located at the tip of fibers displaying GOS values up to 8° (arrow in Figure 11e) and grains of $800 \mu\text{m}$ – 1 mm in size having low GOS values of 3° (e.g., the grain at the bottom of map 4 and bottom left of map 5 in Figures 11e and 12e, respectively).

As in the previous samples, KAM maps confirm the presence of two sets of misorientations within the grains, with misorientation values varying between 0.5° and 1.5° (Figures 11f and 12f). The set oriented perpendicular to the foliation coincides with fluid inclusion bands visible in the optical photos, while the pattern parallel to the foliation coincides with subgrain boundaries. Smaller equant grains are devoid of or only show a few misorientations and are brighter in the optical photos (arrow Figure 12f; compare with Figure 12a).

Pole figures and the ODF of quartz fibers display a maximum for the c-axis at a small angle to X, and two minor maxima coinciding with Z and Y, respectively (subset 1 of map 4 in Figure 11g). In map 5, the c-axes form strong maxima centered on Z in subset 1 and 2, and a maximum at a small angle to X and a weaker maximum close to Y in subset 3 (Figures 12g–12i). The discrete recrystallized domains composed of equant grains form weaker maxima for the c-axis at 45° from X and Z and around Y (subset 2 of map 4 in Figure 11h). The IPF maps document small and equant grains adjacent to the bigger fibers preserving a similar crystallographic orientation as the fiber parent grain, whereas this similarity is not the case for the recrystallized domains (Figures 11j and 12j).

As for the other discussed samples, MAD maps exhibit peaks at values below 10° of correlated grains compatible with a process of subgrain rotation recrystallization and peaks at 60° of misorientation related to Dauphiné twins (Figures 11k and 12k). The uncorrelated grain distribution matches a theoretical (uniform) distribution. A misorientation profile was produced between the edge of a fiber and smaller equant grains. The profile highlights several peaks around 60° for neighboring grains, suggesting that these grains represent former Dauphiné twins (Figures 12f and 12l).

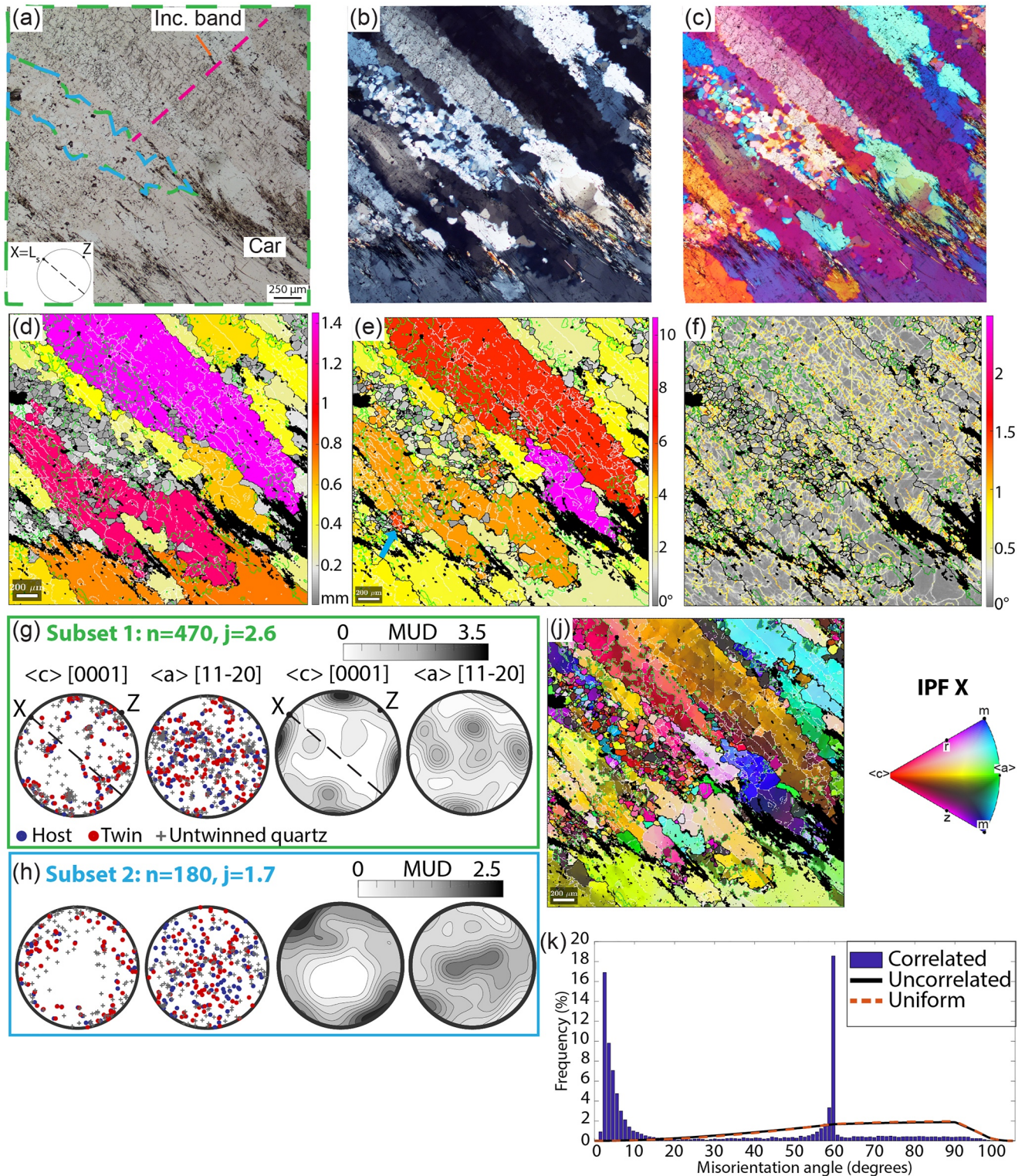


Figure 11. Electron backscatter diffraction (EBSD) map 4 displays quartz and carpholite fibers interfingered (subset 1) and a recrystallized quartz fiber (subset 2). Compare with chemical map of this site in Giuntoli and Viola (2021). (a) Plane-polarized light, (b) crossed-polarized light, and (c) crossed-polarized light with gypsum plate inserted. (d) Quartz grain size map. (e) Quartz grain orientation spread (GOS) map. The blue arrow marks a quartz grain $<200\ \mu\text{m}$ displaying high GOS value. (f) Quartz kernel average misorientation (KAM) map highlights misorientations oriented perpendicular to the foliation coinciding with fluid inclusion bands visible in the optical photos and oriented parallel to the foliation corresponding to subgrain boundaries. Smaller equant grains are devoid of misorientations, as for previous maps. (g–i) Quartz pole figures. (j) IPF map. (k) Misorientation angle distributions (MAD) of quartz grains.

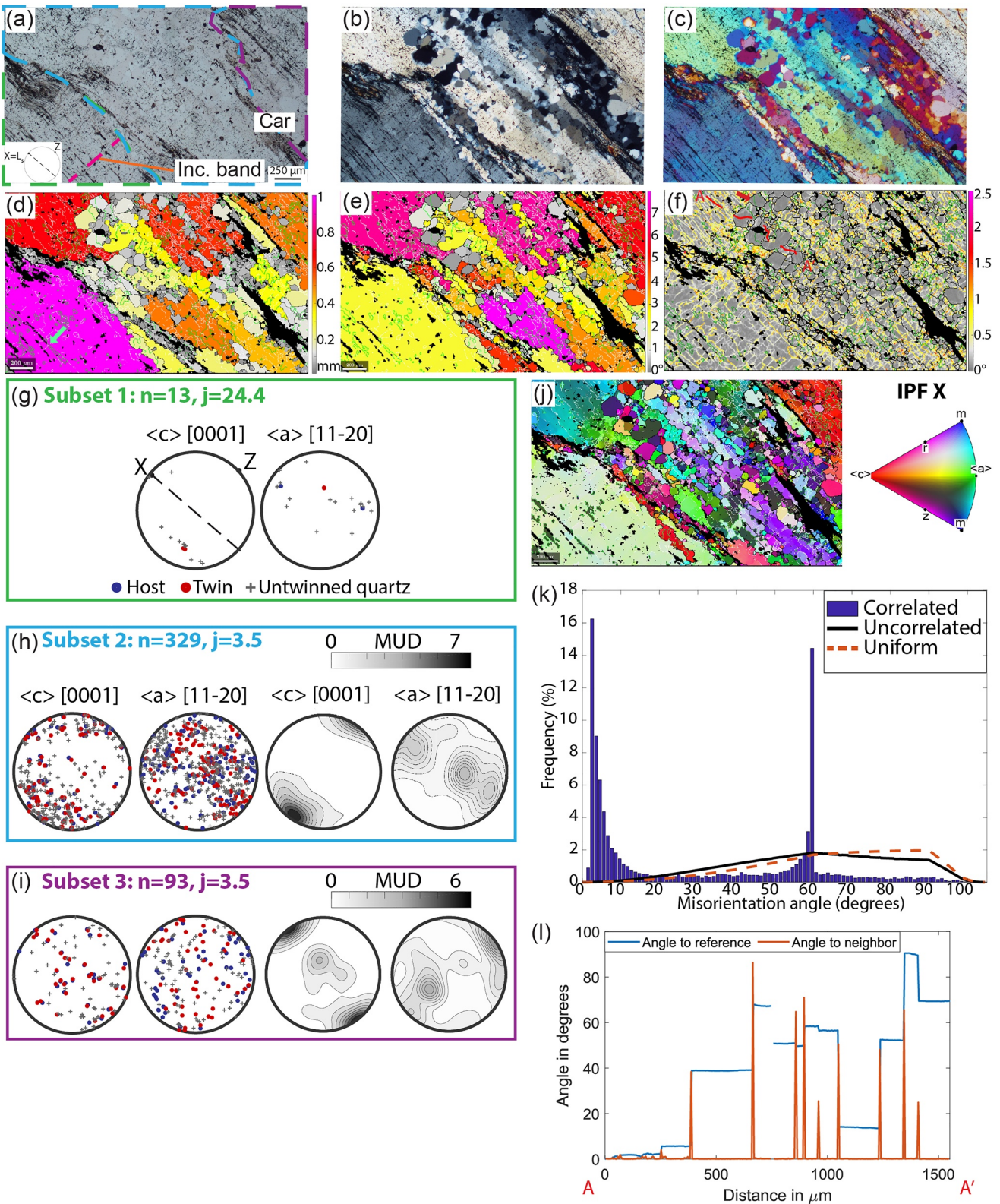


Figure 12.

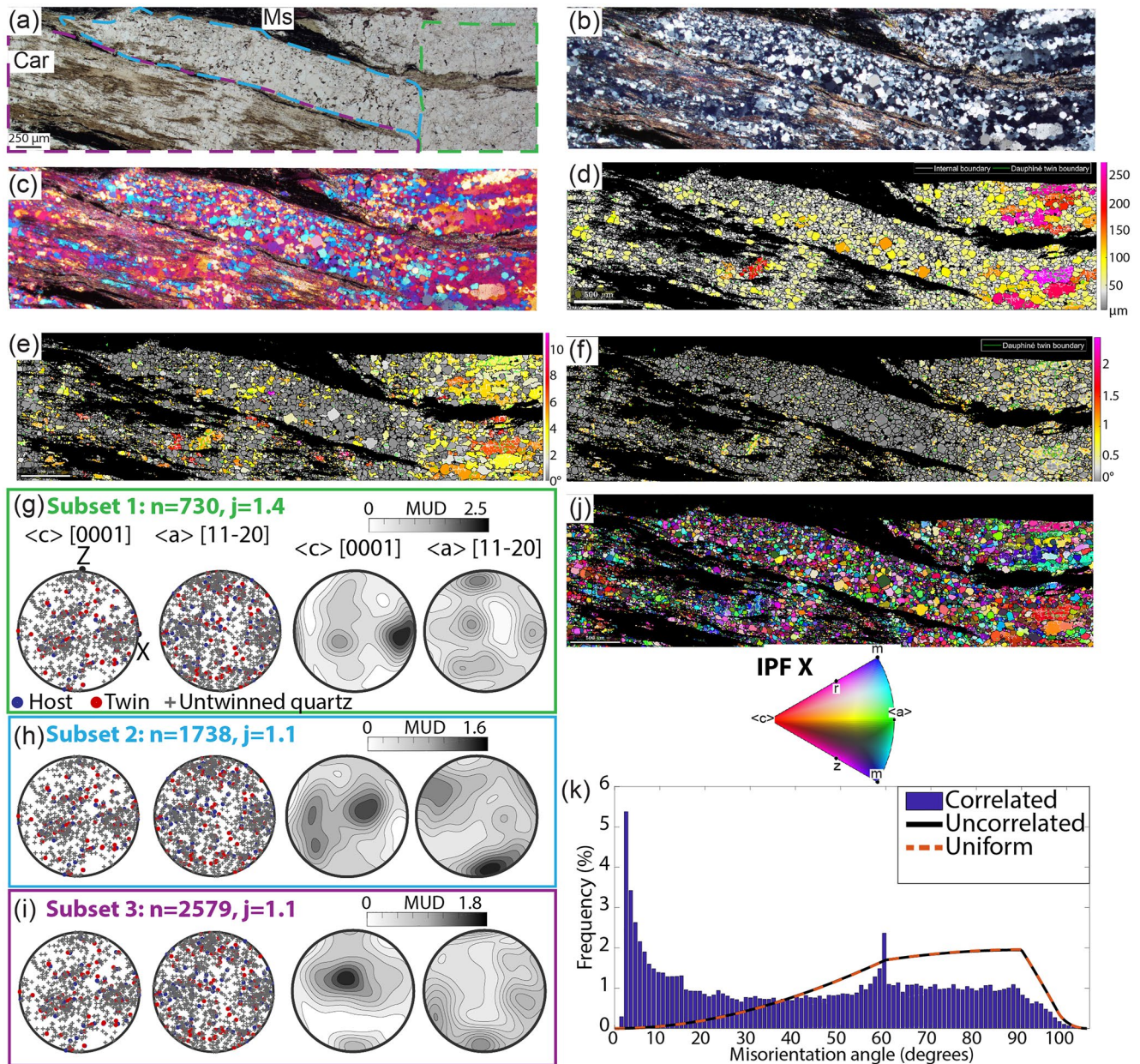


Figure 13. Electron backscatter diffraction (EBSD) map 6 investigating quartz fibers (subset 1), a recrystallized quartz ribbon (subset 2), and a band of quartz, carpholite, and muscovite interfingered (subset 3). (a) Plane-polarized light, (b) crossed-polarized light, and (c) crossed-polarized light with gypsum plate inserted. (d) Quartz grain size map. Note the bigger grain size in subset 1. (e) Quartz grain orientation spread (GOS) map. (f) Quartz kernel average misorientation (KAM) map. (g–i) Quartz pole figures (j) IPF map. (k) Misorientation angle distributions (MAD) of quartz grains.

4.3.2. Recrystallized Quartz Ribbons and Quartz, Carpholite, and Muscovite Layers

These two microstructural domains are described together in this section owing to their spatial relation (see Section 5 for interpretation). Maps 6 and 7 from sample FG1938A and map 8 from sample FG1938C (Figures 13

Figure 12. Electron backscatter diffraction (EBSD) map 5 investigating carpholite grains included inside a quartz fiber (subset 1) and carpholite grains interfingered with partially recrystallized quartz fibers (subsets 2 and 3). (a) Plane-polarized light (b), crossed-polarized light, and (c) crossed-polarized light with gypsum plate inserted. (d) Quartz grain size map. The green arrow shows Dauphiné twins stretched parallel to the lengthening of the fibers and in continuity to carpholite grains. (e) Quartz grain orientation spread (GOS) map. (f) Quartz kernel average misorientation (KAM) map with the trace of the profile trough equant grains devoid of misorientations. (g–i) Quartz pole figures (j) IPF map. (k) Misorientation angle distributions (MAD) of quartz grains. (l) Profile of misorientation from reference point and from neighbor grain.

and 14, respectively) straddle the boundary between either monomineralic quartz ribbons or polymineralic quartz, carpholite, and muscovite layers. In detail, map 6 from sample FG1938A depicts three domains: discrete quartz and carpholite fibers to the right (subset 1), a recrystallized quartz ribbon bounded by carpholite and muscovite grains to the left (subset 2), and a band composed of interfingered quartz, carpholite, and muscovite grains in the bottom left part (subset 3; Figure 13a). The grain size map of subset 1 displays large grains, up to 250 μm , with aspect ratios up to 6, lobate grain boundaries and several subgrains of the same size surrounding equant smaller grains, similar to the centimetre-long quartz fibers (Figure 13d). Subsets 2 and 3 display mostly equant grains <120 μm in size with a few coarser grains characterized by lobate edges and numerous subgrains. All subsets display GOS values up to 8° for the coarse grains and GOS values lower than 2° for grains <120 μm in size (Figure 13e). Some exceptions exist, with grains of 250 μm devoid of subgrains having GOS values of 4° and grains of 100 μm displaying several subgrain and Dauphiné twin boundaries and having GOS values up to 10° with (see Section 5 for a possible interpretation).

The KAM map exhibits several misorientations inside the grains of subset 1, with misorientation values between 0.5° and 1.5° (Figure 13f). The set oriented perpendicular to the foliation coincides spatially with fractures and fluid inclusion bands visible in the optical photos. In all subsets, the smaller equant grains are devoid of these misorientation.

Pole figures and the ODF display a weak CPO in subset 1, with a rather diffuse maximum of c-axes parallel to X and a weaker girdle in the XZ plane (Figure 13g). From subset 1 to 2 and 3 we note a progressive attenuation of CPO, as confirmed by decreasing J-index values (from 1.4 to 1.1; Figures 13g–13i). The small and equant grains adjacent to the coarse grains display similar crystallographic orientation to the parental grains in the IPF maps (Figure 13j). As for the other described maps, the MAD of correlated pairs shows peaks for low angle misorientations (up to 15°) and a peak around 60°, with the uncorrelated pairs distribution following a theoretical random distribution (Figure 13k).

Map 7 in sample FG1938A (Figure 14) contains fine grained carpholite and quartz grains in the top-left area (subset 1), boudinaged carpholite in the center area (subset 2), and quartz grains located between carpholite and muscovite bands in the center-left area (subset 3; Figure 14). Carpholite is boudinaged with smaller carpholite and quartz fibers growing in the neck zone, the bigger of these being enclosed by the white dashed line of Figure 14f. In this area, quartz grains in the vein are elongated parallel to the foliation and display larger grain size (up to 220 μm) and relatively low GOS values than most of the coarse grains (from 1° to 6°, subset 2; Figures 14d and 14e). On the side of subset 2, quartz grains are equant and display finer grain size (<80 μm) and low GOS values (<2°; subsets 1 and 3), although a few quartz grains with high aspect ratios and several subgrain boundaries display GOS value up to 10°–12° and contain several subgrain boundaries. Carpholite acicular grains exert a pinning effect on quartz crystals, as suggested by the sharp and straight grain boundaries of the latter (arrow in Figure 14d; subset 1).

The KAM map highlights misorientations between 0.5° and 1.5° in subset 2, corresponding to fluid inclusion bands visible at the optical microscope (Figure 14f and detail in Figure S2 in Supporting Information S1). Recrystallized grains are devoid of misorientation boundaries (as in the maps discussed above). Pole figures and the ODF display dispersed c-axes values in all subsets, with only weak maxima coinciding with X (Figure 14h). In all subsets, the coarse quartz grains contain at their edges several equant grains sharing similar orientation, as visible from the IPF map and from the optical microphotographs with the gypsum plate, forming ribbons stretched parallel to the foliation (Figure 14j). The MAD of correlated pairs shows peaks at low angle misorientations (<10°) and at around 60°, with uncorrelated pairs distribution following the theoretical random distribution (Figure 14k).

Map 8 in sample FG1938C (Figure 15) shows the boundary between a monomineralic discrete quartz fibers to the right (subset 1), polymineralic quartz and carpholite bands to the top left (subset 2), and a monomineralic band of equant quartz grains to the bottom left (subset 3). In subset 1 quartz grains are coarse (>600 μm) and are elongated parallel to the foliation. They exhibit lobate edges with several subgrains close to the boundaries and equant grains of similar size (<100 μm ; Figure 15). These large grains have generally GOS values <4°, with a few grains with values up to 10° (Figure 15). A decrease in grain size to <200 μm is visible passing from subset 1 to 2 and 3. Subset 2 contains quartz grains characterized by straight contact against carpholite grains. The grains display generally low GOS values, with a few exceptions up to 12°–14° characterized by abundant subgrain boundaries. Subset 3 exhibits equant or slightly elongated grains characterized by maximum GOS values of 4°. The KAM map depicts a correspondence between misorientation values and fluid inclusion bands, especially visible for subset 1 (compare Figures 15a and 15f).

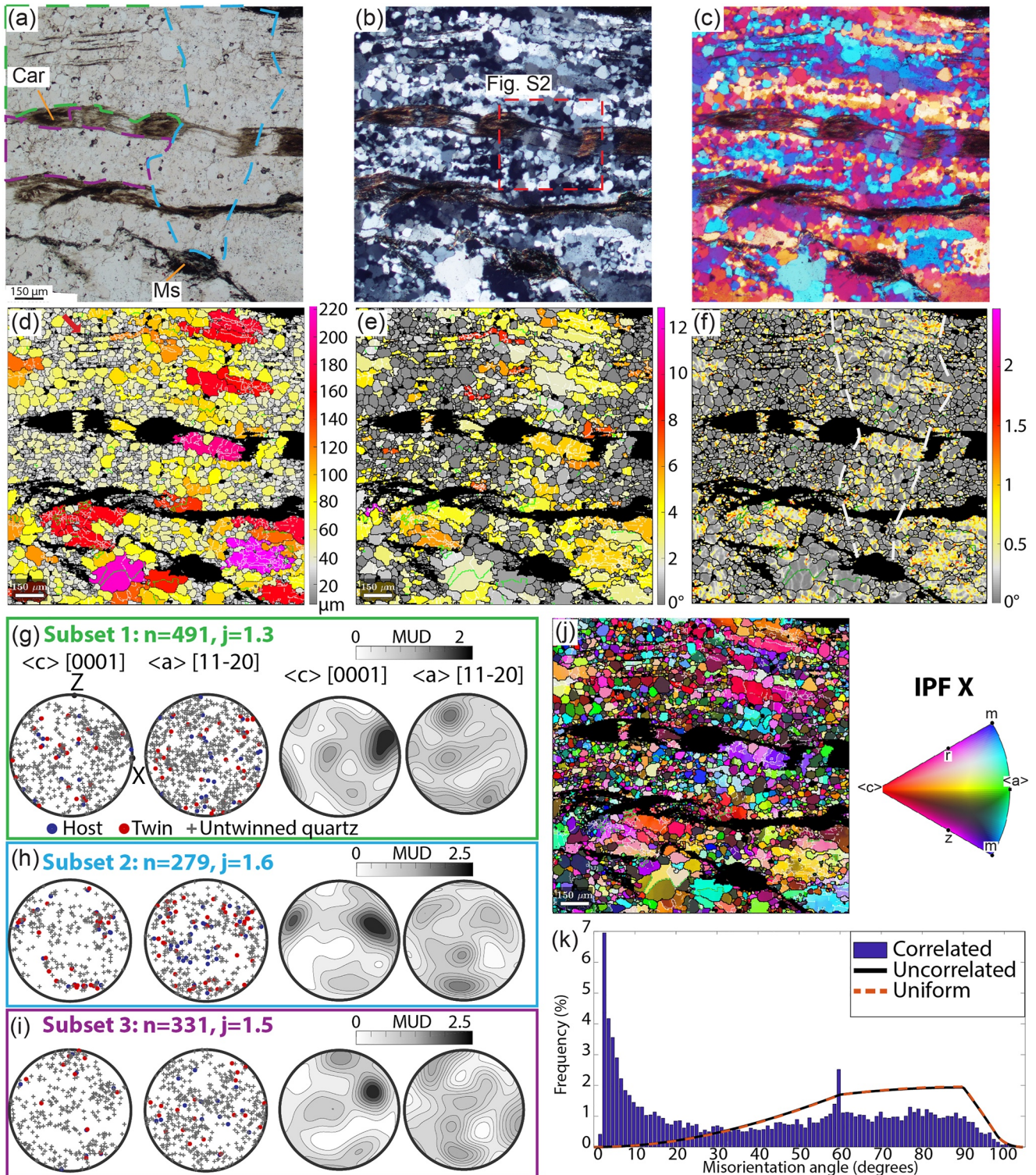


Figure 14. Electron backscatter diffraction (EBSD) map 7 shows fine grained carpholite and quartz grains (subset 1), boudinaged bigger carpholite with quartz fibers growing inside the neck zone (subset 2), and quartz grains located between carpholite and muscovite bands (subset 3). Dashed square: enlargement provided in Figure S2 in Supporting Information S1. (a) Plane-polarized light, (b) crossed-polarized light, and (c) crossed-polarized light with gypsum plate inserted. (d) Quartz grain size map. The arrow indicates carpholite grains pinning quartz grain size. (e) Quartz grain orientation spread (GOS) map. (f) Quartz kernel average misorientation (KAM) map. The bigger neck zone is highlighted by the dashed white line, where misorientations mainly correspond to fluid inclusion bands visible in the optical pictures. (g–i) Quartz pole figures. (j) IPF map. (k) Misorientation angle distributions (MAD) of quartz grains.

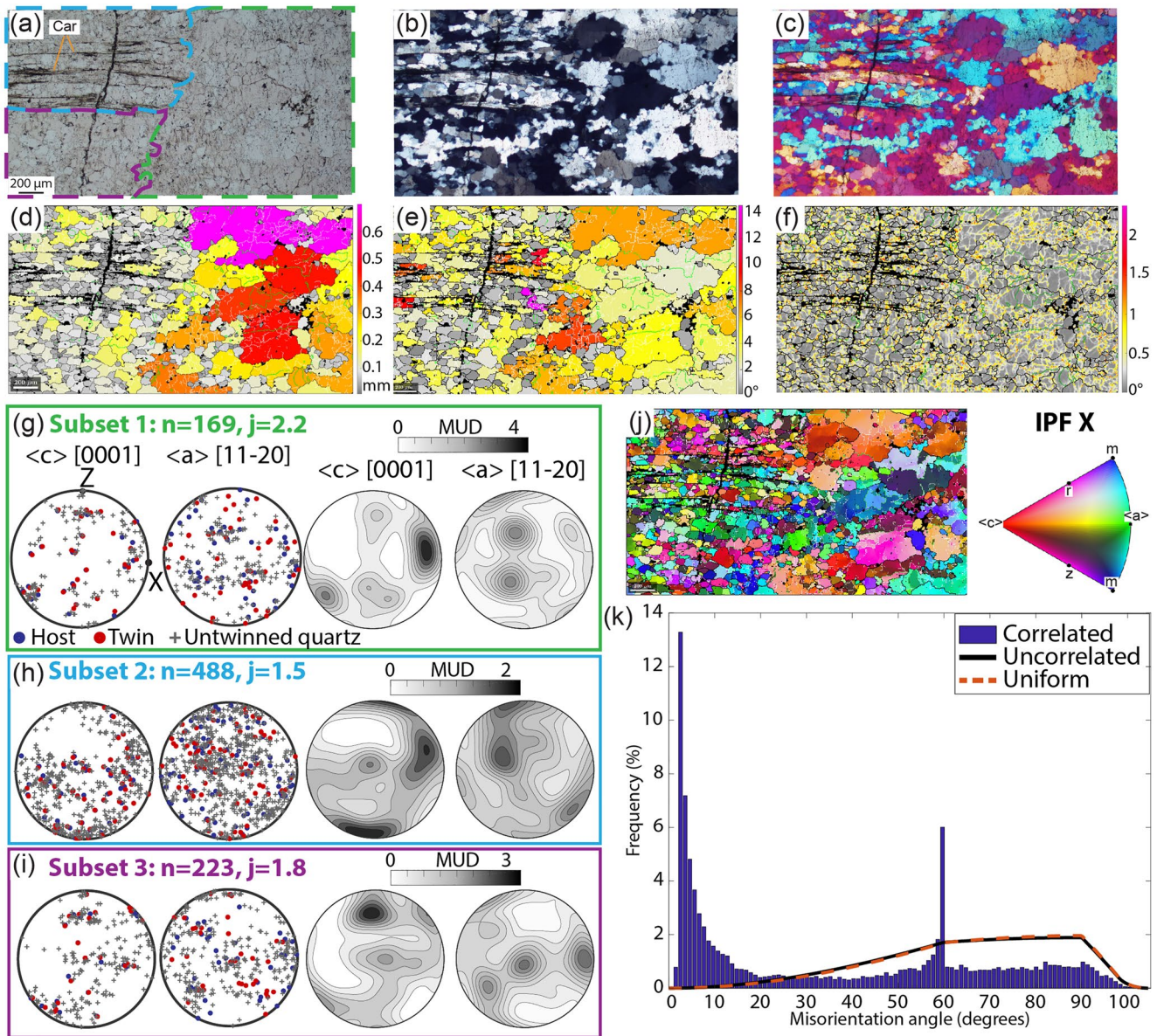


Figure 15. Electron backscatter diffraction (EBSD) map 8 examines the boundary between monomineralic quartz fibers (subset 1), polymineralic quartz and carpholite bands (subset 2), and a monomineralic band of equant quartz grains (subset 3). (a) Plane-polarized light, (b) crossed-polarized light, and (c) crossed-polarized light with gypsum plate inserted. (d) Quartz grain size map. (e) Quartz grain orientation spread (GOS) map. (f) Quartz kernel average misorientation (KAM) map. (g–i) Quartz pole figures. (j) IPF map. (k) Misorientation angle distributions (MAD) of quartz grains.

Pole figures and the ODF constrain a weak CPO for subset 1 and 3, with the c-axis maximum coinciding mainly with X and a secondary cluster lying on the YZ plane for subset 1. In subset 3 the c-axes spread on the YZ plane, whereas subset 2 shows more dispersed orientations (Figures 15g–15i). As in map 7, the IPF map shows how small and equant grains generally preserve an orientation comparable to that of the adjacent coarse grains, forming ribbons strung out parallel to the foliation (Figure 15j). The MAD of correlated pairs shows peaks for misorientations $<10^\circ$ and at around 60° , with uncorrelated pairs distribution following the theoretical random distribution (Figure 15k).

4.4. Differential Stress, Strain Rate, and Failure Mode Diagram

We estimated differential stresses and strain rates for the recrystallized quartz ribbons of FG1925B map 4 subset 2 and FG1938A map 6 subset 2, representing the most recrystallized ribbons in the two samples (Figures 11 and 13; see Section 5.2 for discussion). We used the approach of Cross et al. (2017), with a GOS value of 1.1° used as threshold

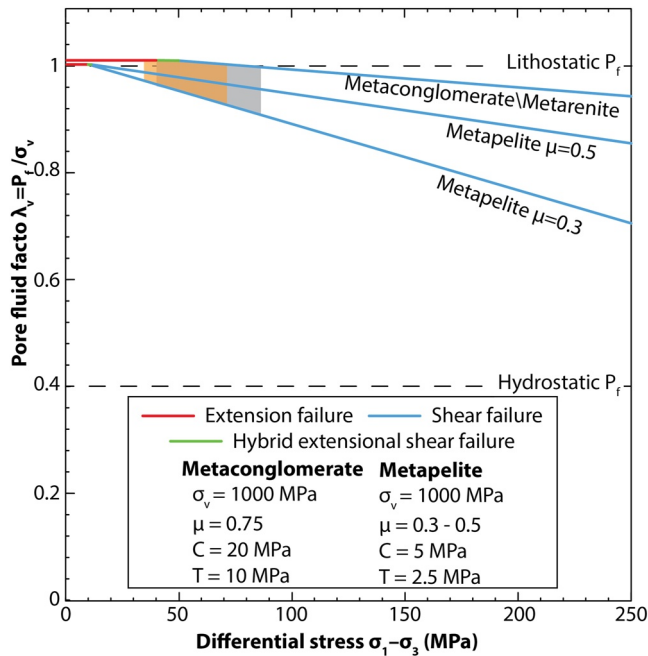


Figure 16. Mohr-Coulomb failure diagram for the studied lithotypes. Differential stress ranges estimated by quartz paleopiezometry are highlighted by the rectangles: gray data from FG1938A (Island of Giglio) and orange data from FG1925 (Farma River).

between relic and recrystallized grains in both samples (Figure S3 in Supporting Information S1). The recrystallized grain size is $41 \pm 21 \mu\text{m}$ (root-mean-squared ± 1 standard deviation) and $28 \pm 14 \mu\text{m}$ in sample FG1925B and FG1938A, respectively, resulting in differential stresses of c. 43 and 55 MPa using the EBSD sliding resolution RMS piezometer (Cross et al., 2017). By referring to the dislocation creep flow law of quartz of Hirth et al. (2001), the resulting strain rates of the recrystallized quartz ribbons are ca. $7 \times 10^{-14} \text{ s}^{-1}$ at 350°C and $6 \times 10^{-13} \text{ s}^{-1}$ at 400°C for sample FG1925B and 10^{-13} s^{-1} at 350°C and 10^{-14} s^{-1} at 300°C for sample FG1938A.

We computed failure mode diagrams (Cox, 2010) for the three different lithotypes observed in the field (metaconglomerate, metarenite, and metapelite) using the differential stress ranges obtained from the recrystallized grain sizes ± 1 standard deviation of the two samples. The resulting failure mode diagrams for the metaconglomerate and metarenite indicate failure modes varying from extension failure to hybrid and shear failure in sample FG1925B and from hybrid to shear failure in FG1938A, with λ_v from close to exceeding lithostatic values (Figure 16). Failure mode diagrams for the metapelite in both samples indicate shear failure for λ_v values between 0.95 and 0.99.

5. Discussion

5.1. Deformation Mechanisms of Dilational Hydroshear Veins

Dilational hydroshear veins formed at blueschist facies conditions of $>1 \text{ GPa}$ and 300–350°C both at the Island of Giglio and the Farma River (data from Giuntoli & Viola, 2021, 2022). In the dilational hydroshear veins quartz fibers are characterized by various degrees of deformation and recrystallization as a function of the microstructural domain they belong to, as presented in Section 4.3 (Figure 5). Large fibers generally display low GOS values, indicative of low deformation. Fibers experienced only local grain size reduction by subgrain rotation recrystallization, as indicated by the MAD maps displaying strong peaks for correlated pairs at low angle misorientations (between 2° and 10°) and by the high J-indexes, suggesting that adjacent grains are characterized by low mutual angular relationships wherein crystallographic inheritance from the parent grain is strong in the new grain (Neumann, 2000; Wheeler et al., 2001, Figures 8–15). Grain size reduction by subgrain rotation recrystallization is also confirmed by the similar size of both the subgrains and the newly formed equant grains. The MAD peak around 60°, on the other hand, is associated with Dauphiné twinning (Lloyd, 2004; Menegon et al., 2011). Subgrain rotation recrystallization can be partly favored by Dauphiné twins formed in response to deformation, as suggested by the twins size similar to subgrains and equant grains and by the abundance of Dauphiné twins in proximity of recrystallized domains (Lloyd, 2004; Menegon et al., 2011). This interpretation is also supported by the misorientation profile of map 5 (Figures 12f and 12l). Moreover, Dauphiné twins are also observed to follow carpholite acicular grains included in the quartz fibers (green arrow in Figure 12d).

KAM maps highlight misorientations between 0.5° and 1° that mostly mimic a dense set of sealed microfractures decorated by fluid inclusions oriented at high angle to the fiber lengthening direction, as visible in the corresponding optical microphotographs (e.g., Figures 11a and 11f). This wealth of fluid inclusions likely reflects the abundance of fluid during dilational hydroshearing and veining by crack-and-sealing (e.g., Cox & Etheridge, 1983; Durney & Ramsay, 1973, Figures 17a and 17b). It is noteworthy that the recrystallized equant quartz grains contain neither fluid inclusion bands nor sealed microfractures, suggesting that recovery recrystallization promoted fluid expulsion from the recrystallizing quartz crystal lattice (Faleiros et al., 2010; Finch et al., 2016; Kerrich, 1976; Trepmann et al., 2010; arrow in Figure 12f). Additionally, microfracturing could also promote grain size reduction, followed by healing by strain-induced grain boundary migration (e.g., Lagoeiro & Barbosa, 2010; Trepmann et al., 2007).

Quartz fibers have their c-axis mainly coinciding with the X strain axis, and to a lesser extent with Z, likely due to quartz fast growth along the c-axis direction (Bons & den Brok, 2000; Hippert, 1994; Trepmann & Seybold, 2019, Figures 9g, 10g and 11g). Moreover, fibers with their c-axis coinciding or oriented at a small angle to X may imply that they were less prone to recrystallization, due to their unfavorable orientation for the

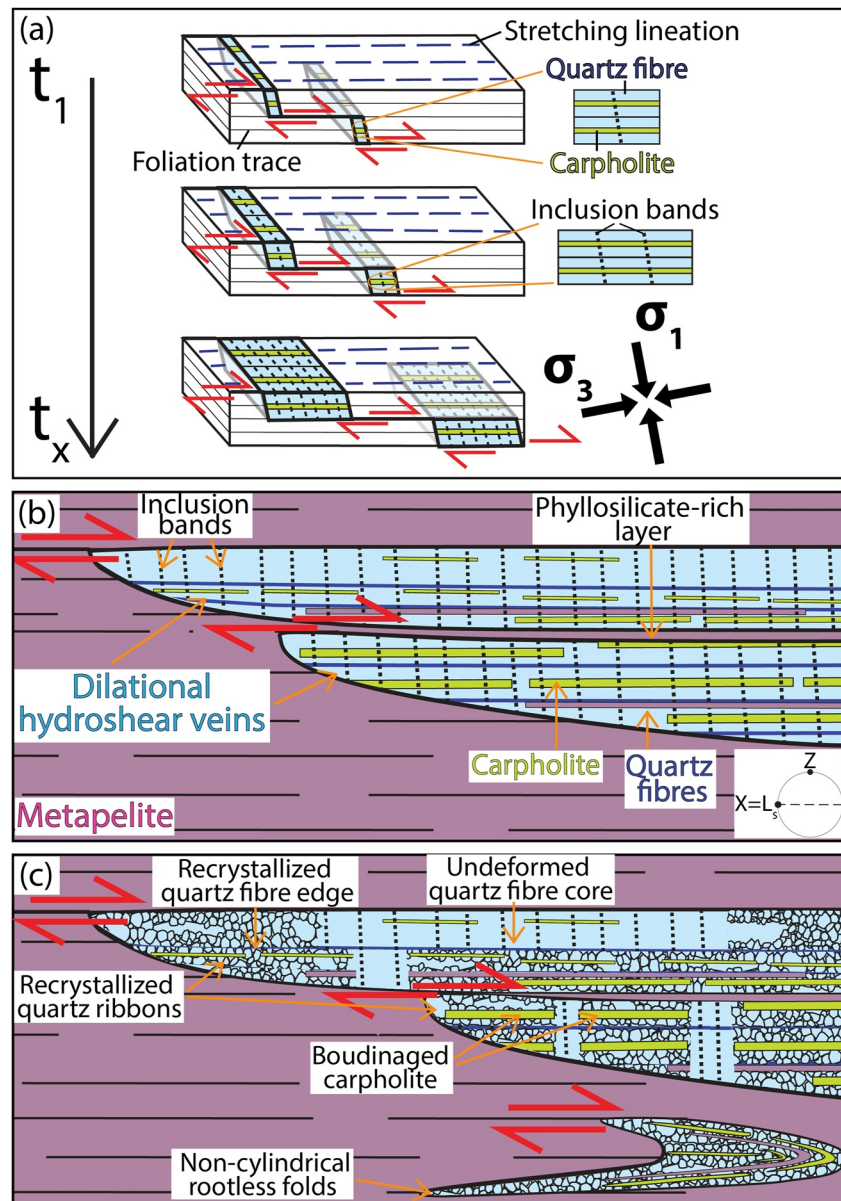


Figure 17. Conceptual sketch illustrating the formation and progressive deformation of dilational hydroshear veins. (a) Formation of dilational hydroshear veins by incremental crack-and-seal growth steps, the orientation of the greatest and least compressive stresses σ_1 and σ_3 is displayed. (b) Detailed sketch of the microstructures of dilational hydroshear veins. (c) Microstructures of dilational hydroshear veins after deformation (see text for discussion).

activation of the (c) $\langle a \rangle$, $\{m\} \langle a \rangle$, and $\{m\} \langle c \rangle$ slip systems (e.g., Neumann, 2000), except for prism-slip $\{m\} \langle c \rangle$, which is generally active at higher temperature than that estimated for those structures (Stipp et al., 2002b). Therefore, the resulting CPO is compatible with oriented grain growth and is not the result of later deformation by dislocation creep (e.g., Ceccato et al., 2017; Giuntoli et al., 2018; Pennacchioni et al., 2010; Price et al., 2016; Spruzeniece et al., 2017). Grain size reduction, recrystallization, phase mixing, and pinning occurred preferentially where other phases were present and where quartz fibers are thinner (microstructural domains 2 and 3 in Section 4.3, Figures 13 and 14 and Figure 15). Additionally, in the recrystallized quartz ribbons a transition from dislocation to diffusion creep by grain boundary sliding might be suggested by the attenuation and dispersion of CPO in FG1938A map 6 (Figures 13g–13i; Ceccato et al., 2017; Gilgannon et al., 2017; Giuntoli et al., 2020; Kilian et al., 2011; Menegon et al., 2015; Viegas et al., 2016) and by the diamond shape of numerous recrystallized grains (e.g., Drury & Humphreys, 1988; Fliervoet et al., 1997; White, 1977).

Summarizing, EBDS data indicate that quartz single-grain fibers display a low amount of strain and recrystallization, mostly limited to the lateral termination of the fibers producing recrystallized ribbons (Figure 17c). Hence, quartz fibers acted as competent domains, potentially also due to the carpholite inclusions that strengthened the quartz grains. The little recrystallization and deformation of quartz fibers occurred primarily by subgrain rotation recrystallization, likely assisted at higher strain by diffusion creep by grain boundary sliding. These processes are preferentially observed where quartz fibers are thinner, with a favorable crystallographic orientation and carpholite and muscovite also occur, thus suggesting a compositional control and strain partitioning reflecting the different mineralogical composition of the multigrain bands.

Locally, effects of non-coaxial folding and rootless folds are visible from the meso-to the micro-scale and deforms dilational hydroshear veins (Figures 4d–4f, 6d–6f and 7e–7h). These folds are spatially confined to quartz-rich bands bounded by phyllosilicate layers, whereas adjacent quartz bands contain almost undeformed quartz fibers (top parts of Figures 6d–6f and 7e–7f). Based on these observations, we believe that deformation was preferentially accommodated by slip mostly along phyllosilicate bands, which acted as weak slip surfaces and as decollement horizons, as suggested for similar veins found in shallower geological settings (De Roo & Weber, 1992; Fagereng et al., 2010; Koehn & Passchier, 2000; Labaume et al., 1991, Figure 17c). This interpretation is also supported by numerous literature examples indicating that phyllosilicates can accommodate large amounts of deformation by slip on their basal planes (e.g., Bos & Spiers, 2001; Giuntoli et al., 2020; Kronenberg, 1990; Mariani et al., 2006; Shea & Kronenberg, 1993; Wintsch et al., 1995) and through ripplocation motion (Aslin et al., 2019; Kushima et al., 2015). Adjacent metaquartzarenite and metaconglomerate bodies deformed mainly by dissolution-precipitation creep, a deformation mechanism that accommodates high strain rates at low differential stresses (e.g., Bos & Spiers, 2002; Condit et al., 2022; Platt et al., 2018; Treppmann & Seybold, 2019, Figure 3), although also dislocation creep played a secondary role especially in the monomineralic quartz bands.

5.2. Differential Stress, Strain Rate, Failure Mode, and Implications for Deep ETS

In quartz-rich rocks, caution should be taken when applying quartz paleopiezometry and using quartz flow laws if phyllosilicate are present, as the resulting differential stresses and strain rates might be drastically affected by the presence and the degree of physical interconnectivity of weak phyllosilicates acting as easy-glide planes (e.g., Bukovská et al., 2016; Hunter et al., 2016; Menegon, Pennacchioni, Heilbronner, & Pittarello, 2008). As presented in Section 4.3, recrystallized quartz ribbons are sandwiched between muscovite and carpholite-rich bands. Locally, incipient boudinage is visible, involving stronger quartz lithons in-between weaker muscovite bands, both at the hand sample- and field scale (Figure 5a). Thus, the 43 and 55 MPa differential stresses computed in this study from quartz paleopiezometry represent only upper bound constraints, likely limiting the system bulk differential stress to lower values (e.g., Gardner et al., 2016). On the contrary, the obtained strain rates between 10^{-13} and 10^{-14} s⁻¹ might represent a lower bound, as the same differential stresses would indicate faster strain rates using the flow laws for muscovite (Mares & Kronenberg, 1993; Mariani et al., 2006). The estimated strain rates are in the order of geological and geodetical estimates of bulk finite strains (Fagereng & Biggs, 2019; Pfiffner & Ramsay, 1982; see interpretation in the proposed model below).

Failure mode diagrams indicate pore fluid factors values close to or exceeding lithostatic values in the host metapelite and metaconglomerate-metaquartzarenite, respectively (Figure 16). Extension and hybrid failure are predicted to occur at lower differential stresses in the metapelite than in the metaconglomerate-metaquartzarenite. As described in Section 4, dilational hydroshear veins formed preferentially in the metapelite, while Mode I veins occur almost exclusively in metaquartzarenite and metaconglomerate (see also Giuntoli & Viola, 2021, 2022 for further details). Thus, field data partially agree with the theoretical failure mode diagrams predicting extension failure to only occur in the metaconglomerate and metaquartzarenite. On the other hand, they disagree in that hybrid shearing occurs in the metapelite although it is not predicted by the theoretical considerations shown by the diagram. This difference is consistent with what was discussed above, that is, that differential stresses obtained by quartz paleopiezometry represent an upper bound, given that with lower differential stresses hybrid fracturing would be promoted also in the metapelite. Nonetheless, the failure mode diagram suggests that lithological interfaces are loci where similar differential stresses can result in different failure modes.

The described dilational hydroshear veins are up to several meters long and contain fluid inclusion bands a few tens of microns apart in the least deformed fibers (Section 4). According to Fagereng et al. (2011) and Ujjié et al. (2018), the fluid inclusion band spacing in the fibers tracks repeated slip increments. Using the equation

$\frac{u}{L} = \frac{\Delta\tau}{G}$ (Wells & Coppersmith, 1994), where u is the slip, L is the potential rupture length, $\Delta\tau$ is the stress drop, and G is the shear modulus (3 GPa for underthrust metasediments; Takahashi et al., 2002), the stress drops computed for the studied structures are in the order of a few kPa to a few tens of kPa. These results are compatible with the low stress drops observed for ETS (1–100 kPa; e.g., Ito & Obara, 2006; D. A. Schmidt & Gao, 2010) and with values estimated from fossil structures (Fagereng et al., 2011; Ujiie et al., 2018).

Our results are thus consistent with the model for ETS formation proposed by Bernaudin and Gueydan (2018) and can be related to three main deformation stages: (a) aseismic creep, (b) tremor and slow slip, and (c) fracture sealing (Figure 18). (a) In the studied samples, aseismic creep occurred preferentially via dissolution-precipitation creep in the metaconglomerate and metaquartzarenite, slip on the basal plane of phyllosilicate in metapelite and by dislocation creep with subgrain rotation recrystallization and diffusion creep in the quartz dilational hydroshear veins. The estimated differential stresses and strain rates record this stage. (b) Tremors would have caused meso and micro-fracturing as visible both in the field and in thin section and caused by transient high pore fluid pressure cyclically reaching supralithostatic values. Slow slip could be the effect of preferential slip on phyllosilicate bands. Differently from Bernaudin and Gueydan (2018) who studied granitic rocks, we propose that slow-slip in phyllosilicate-rich rocks may be mainly accommodated by slip along phyllosilicate-rich bands. (c) The produced fractures increased the porosity of the rock volume and allowed for fluid ingress, migration, and venting, with the subsequent formation of synkinematic minerals. These three stages repeated cyclically in time, as did the fluctuations of pore pressure.

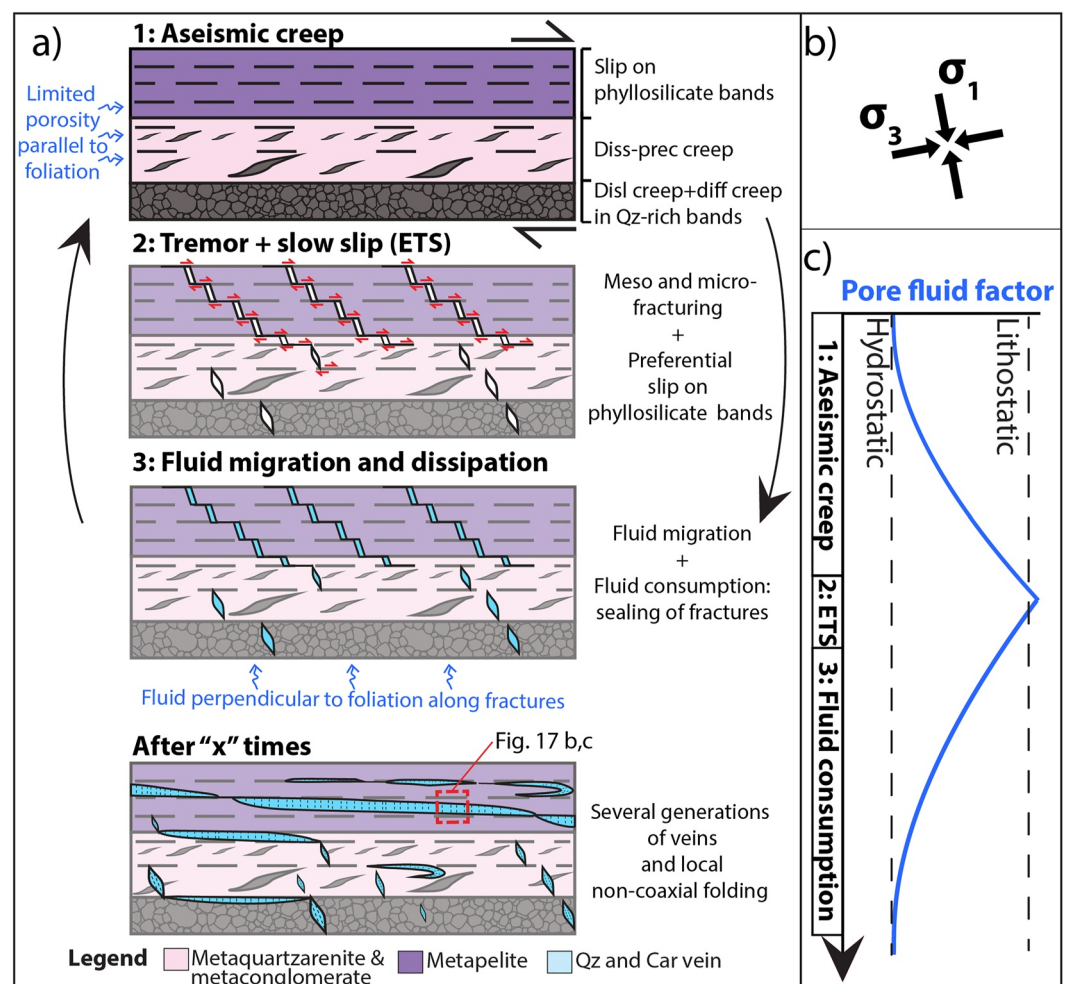


Figure 18. (a) Sketch of the proposed conceptual model for the deformation mechanisms of deep episodic tremor and slow slip events (ETS). Stages 1–3 repeat cyclically, with the last cartoon representing the situation after “x” cycles. Qz: quartz. (b) The orientation of the greatest and least compressive stresses σ_1 and σ_3 is displayed. (c) Simplified evolution of pore fluid factor during the three stages described in (a).

Transient high pore pressure could be sustained by the phyllosilicate bands that acted as sealing horizons (e.g., Ganzhorn et al., 2019), constraining fluid flow along the anisotropy of the foliation. However, fracturing could break the phyllosilicate seals, thus creating fluid pathways across the foliation, similarly to the fault-valve model (Sibson, 1990, 2013) and to what has been proposed for ETS (Gosselin et al., 2020; Nakajima & Uchida, 2018; Warren-Smith et al., 2019). Additionally, at the Island of Giglio, quartz and carpholite fibers in dilational hydroshear veins display different orientations on different bands located a few centimeters away across the main foliation, suggesting coeval and/or diachronous slip on different subparallel planes (Figures 4a–4c; e.g., Kirkpatrick et al., 2021), although we cannot exclude that the different orientations of fibers stem from later transposition.

Rheological heterogeneities are believed to be a characteristic feature of deep ETS (e.g., Behr et al., 2018; Hayman & Lavier, 2014; Kotowski & Behr, 2019; Platt et al., 2018). The two studied localities show similar microstructural deformation mechanisms but different mesoscopic deformation. In detail, at the Island of Giglio deformation and shearing produced a broken formation (as defined in Festa et al., 2019; Hsü, 1968), with rheologically strong metaconglomerate and metarenite blocks and boudins embedded in a weaker metapelite matrix, with the metapelite layers acting as weak horizons that allowed shearing and transposition (Giuntoli & Viola, 2022). This is not the case in the MRU, where a mesoscopic compressional duplex is composed of imbricated stronger metaquartzarenite horses surrounded by weaker metapelite higher strain zones (Giuntoli & Viola, 2021). As a consequence, in the latter more rheological coherence was maintained during deformation, possibly because the ratio between weak metapelite and strong metaquartzarenite is lower compared to the Island of Giglio. As described in Section 4.1, veins are longer and more abundant at the Island of Giglio compared to the Farma River, with possible consequences upon fluid compartmentalization and potential overpressure. Thus, the primary sedimentary differences between rheologically strong metaquartzarenite and metaconglomerate and weaker metapelite control the overall style of deformation and the degree of coherence of compositionally heterogeneous multilayer metasedimentary formations. Rheological differences among metasedimentary formations might also impact the seismological style and signal, for example, by influencing the spatial distribution of seismic failures, their size and recurrence time.

6. Conclusions

We investigated dilational hydroshear veins formed in continental metasediments at blueschist facies conditions (350–400°C, ~1 GPa). Samples are from two localities situated more than 80 km apart, along a transect covering the entire width of the Tuscan Metamorphic Units (Northern Apennines, Italy), but exhibit strikingly similar meso- and microstructures. Microstructural and EBSD analyses of dilational hydroshear veins show only local recrystallization of the vein quartz fibers by subgrain rotation recrystallization, likely followed by diffusion creep by grain boundary sliding. We estimated differential stresses of 43–55 MPa and strain rates between 10^{-13} and 10^{-14} s⁻¹ from the recrystallized quartz fibers. Thus, dilational hydroshear veins are slightly deformed, suggesting that surrounding metapelite bands accommodated most of the deformation acting as decollement horizons. Nearby metaconglomerates and metaquartzarenites deformed mainly by dissolution-precipitation creep. Meso- and microstructural analysis and failure mode diagrams indicate pore factors values near to or exceeding lithostatic values.

We suggest that the observed microstructures and deformation mechanisms are a geological record of deep episodic tremor and slow slip events in a continental metasedimentary formation. We propose a model where pore pressure cyclically reached supralithostatic values triggering tremors and inducing fracturing of all lithotypes. Slow slip was accommodated preferentially by slip on phyllosilicate bands. Fluid was drained due to fluid migration in the increased porosity and to partial fluid consumption due to hydrous mineral precipitation in syn-deformation veins. Successive aseismic creep occurred via dislocation creep with subgrain rotation recrystallization in the quartz dilational hydroshear veins, slip on the basal plane of phyllosilicate and mainly by dissolution and precipitation creep in the host rock. We propose that metapelite horizons can act as seal horizons that can sustain transient high pore pressure, limiting fluid flow parallel to the foliation except when fracturing occurs.

Data Availability Statement

The data presented in the manuscript are available in the main text, figures, Supporting Information S1, in the references and in the Mendeley Data repository (<https://data.mendeley.com/datasets/d238p54v6g/2>; Giuntoli et al., 2022). The Matlab toolbox MTEX (Bachmann et al., 2010, 2011; Mainprice et al., 2015) version 5.8.0 was used to process the EBSD data (<https://mtex-toolbox.github.io/>).

Acknowledgments

A. Ceccato and L. Menegon are acknowledged for fruitful discussions. We acknowledge the constructive comments and suggestions by Whitney M. Behr and an anonymous reviewer and Yves Bernabe for the editorial handling. This project has received funding from the European Union's Horizon 2020 research and innovation programme under the Marie Skłodowska-Curie grant agreement N° 839779. Open Access Funding provided by Università degli Studi di Bologna within the CRUI-CARE Agreement.

References

- Angiboust, S., Kirsch, J., Oncken, O., Glodny, J., Monié, P., & Rybacki, E. (2015). Probing the transition between seismically coupled and decoupled segments along an ancient subduction interface. *Geochemistry, Geophysics, Geosystems*, 16(6), 1905–1922. <https://doi.org/10.1002/2015gc005776>
- Aslin, J., Mariani, E., Dawson, K., & Barsoum, M. W. (2019). Ripplifications provide a new mechanism for the deformation of phyllosilicates in the lithosphere. *Nature Communications*, 10(1), 686. <https://doi.org/10.1038/s41467-019-08587-2>
- Audet, P., Bostock, M. G., Christensen, N. I., & Peacock, S. M. (2009). Seismic evidence for overpressured subducted oceanic crust and megathrust fault sealing. *Nature*, 457(7225), 76–78. <https://doi.org/10.1038/nature07650>
- Azzaro, E., Cocozza, T., Di Sabatino, B., Gasperi, G., Gelmini, R., Lazzarotto, A., et al. (1976). Geology and petrography of the Verrucano and Paleozoic formations of southern Tuscany and northern Latium (Italy). In H. Falke (Ed.), *The continental Permian in central, west, and south Europe* (pp. 181–195). Springer Netherlands. https://doi.org/10.1007/978-94-010-1461-8_15
- Bachmann, F., Hielscher, R., & Schaeben, H. (2010). Texture analysis with MTEX—free and open source software toolbox. In *Solid state phenomena* (Vol. 160, pp. 63–68). Trans Tech Publication. <https://doi.org/10.4028/www.scientific.net/ssp.160.63>
- Bachmann, F., Hielscher, R., & Schaeben, H. (2011). Grain detection from 2d and 3d EBSD data—Specification of the MTEX algorithm. *Ultra-microscopy*, 111(12), 1720–1733. <https://doi.org/10.1016/j.ultramic.2011.08.002>
- Barnes, P. M., Wallace, L. M., Saffer, D. M., Bell, R. E., Underwood, M. B., Fagereng, A., et al. (2020). Slow slip source characterized by lithological and geometric heterogeneity. *Science Advances*, 6(13), eaay3314. <https://doi.org/10.1126/sciadv.aay3314>
- Behr, W. M., & Bürgmann, R. (2021). What's down there? The structures, materials and environment of deep-seated slow slip and tremor. *Philosophical Transactions of the Royal Society A: Mathematical, Physical & Engineering Sciences*, 379(2193), 20200218. <https://doi.org/10.1098/rsta.2020.0218>
- Behr, W. M., Kotowski, A. J., & Ashley, K. T. (2018). Dehydration-induced rheological heterogeneity and the deep tremor source in warm subduction zones. *Geology*, 46(5), 475–478. <https://doi.org/10.1130/g40105.1>
- Bell, T. H., Rubenach, M. J., & Fleming, P. D. (1986). Porphyroblast nucleation, growth and dissolution in regional metamorphic rocks as a function of deformation partitioning during foliation development. *Journal of Metamorphic Geology*, 4(1), 37–67. <https://doi.org/10.1111/j.1525-1314.1986.tb00337.x>
- Bernaudin, M., & Gueydan, F. (2018). Episodic tremor and slip explained by fluid-enhanced microfracturing and sealing. *Geophysical Research Letters*, 45(8), 3471–3480. <https://doi.org/10.1029/2018GL077586>
- Beroza, G. C., & Ide, S. (2011). Slow earthquakes and nonvolcanic tremor. *Annual Review of Earth and Planetary Sciences*, 39(1), 271–296. <https://doi.org/10.1146/annurev-earth-040809-152531>
- Bianco, C., Godard, G., Halton, A., Brogi, A., Liotta, D., & Caggianelli, A. (2019). The lawsonite-glaucophane blueschists of Elba Island (Italy). *Lithos*, 348, 105198. <https://doi.org/10.1016/j.lithos.2019.105198>
- Bilek, S. L., & Lay, T. (2018). Subduction zone megathrust earthquakes. *Geosphere*, 14(4), 1468–1500. <https://doi.org/10.1130/GES01608.1>
- Bons, P. D., & denBrok, B. (2000). Crystallographic preferred orientation development by dissolution–precipitation creep. *Journal of Structural Geology*, 22(11), 1713–1722. [https://doi.org/10.1016/s0191-8141\(00\)00075-4](https://doi.org/10.1016/s0191-8141(00)00075-4)
- Bons, P. D., Elburg, M. A., & Gomez-Rivas, E. (2012). A review of the formation of tectonic veins and their microstructures. *Journal of Structural Geology*, 43, 33–62. <https://doi.org/10.1016/j.jsg.2012.07.005>
- Bos, B., & Spiers, C. J. (2001). Experimental investigation into the microstructural and mechanical evolution of phyllosilicate-bearing fault rock under conditions favouring pressure solution. *Journal of Structural Geology*, 23(8), 1187–1202. [https://doi.org/10.1016/S0191-8141\(00\)00184-X](https://doi.org/10.1016/S0191-8141(00)00184-X)
- Bos, B., & Spiers, C. J. (2002). Frictional-viscous flow of phyllosilicate-bearing fault rock: Microphysical model and implications for crustal strength profiles. *Journal of Geophysical Research*, 107(B2), EC V1–1–ECV1-13. <https://doi.org/10.1029/2001jb000301>
- Brogi, A., & Giorgetti, G. (2012). Tectono-metamorphic evolution of the siliciclastic units in the middle Tuscan range (inner northern Apennines): Mg–carpholite bearing quartz veins related to syn-metamorphic syn-orogenic foliation. *Tectonophysics*, 526, 167–184. <https://doi.org/10.1016/j.tecto.2011.09.015>
- Bukovská, Z., Jeřábek, P., & Morales, L. F. G. (2016). Major softening at brittle-ductile transition due to interplay between chemical and deformation processes: An insight from evolution of shear bands in the South Armorican Shear Zone. *Journal of Geophysical Research: Solid Earth*, 121(2), 1158–1182. <https://doi.org/10.1002/2015JB012319>
- Bunge, H.-J. (2013). *Texture analysis in materials science: Mathematical methods*. Elsevier.
- Carminati, E., & Doglioni, C. (2012). Alps vs. Apennines: The paradigm of a tectonically asymmetric Earth. *Earth-Science Reviews*, 112(1), 67–96. <https://doi.org/10.1016/j.earscirev.2012.02.004>
- Casini, G., Decandia, F. A., & Tavarnelli, E. (2007). Analysis of a mesoscopic duplex in SW Tuscany, Italy: Implications for thrust system development during positive tectonic inversion. *Geological Society, London, Special Publications*, 272(1), 437–446. <https://doi.org/10.1144/gsl.sp.2007.272.01.22>
- Casini, G., Decandia, F. A., & Tavarnelli, E. (2008). Pre-orogenic extensional deformations within Permian-Triassic rocks of Southern Tuscany: Structural record of an episode of Early Mesozoic continental rifting? *Bollettino della Società Geologica Italiana*, 127(3), 615–624.
- Ceccato, A., Pennacchioni, G., Menegon, L., & Bestmann, M. (2017). Crystallographic control and texture inheritance during mylonitization of coarse grained quartz veins. *Lithos*, 290–291, 210–227. <https://doi.org/10.1016/j.lithos.2017.08.005>
- Chapman, J. S., & Melbourne, T. I. (2009). Future Cascadia megathrust rupture delineated by episodic tremor and slip. *Geophysical Research Letters*, 36(22). <https://doi.org/10.1029/2009gl040465>
- Chen, Y., Hjelen, J., Gireesh, S. S., & Roven, H. J. (2012). Optimization of EBSD parameters for ultra-fast characterization. *Journal of Microscopy*, 245(2), 111–118. <https://doi.org/10.1111/j.1365-2818.2011.03551.x>

- Condit, C. B., & French, M. E. (2022). Geologic evidence of lithostatic pore fluid pressures the base of the subduction seismogenic zone. *Geophysical Research Letters*, 49(12), e2022GL098862. <https://doi.org/10.1029/2022GL098862>
- Condit, C. B., French, M. E., Hayles, J. A., Yeung, L. Y., Chin, E. J., & Lee, C.-T. A. (2022). Rheology of metasedimentary rocks at the base of the subduction seismogenic zone. *Geochemistry, Geophysics, Geosystems*, 23(2), e2021GC010194. <https://doi.org/10.1029/2021GC010194>
- Conti, P., Cornamusini, G., & Carmignani, L. (2020). An outline of the geology of the northern Apennines (Italy), with geological map at 1:250,000 scale. *Italian Journal of Geosciences*, 139(2), 149–194. <https://doi.org/10.3301/ijg.2019.25>
- Costantini, A., Decandia, F. A., Lazzarotto, A., & Sandrelli, F. (1988). L'unità di Monticiano-Roccastrada fra la Montagnola senese ed il Monte Leoni (Toscana meridionale). *Atti Ticinensi di Scienze della Terra*, 31, 382–420.
- Cox, S. F. (2010). The application of failure mode diagrams for exploring the roles of fluid pressure and stress states in controlling styles of fracture-controlled permeability enhancement in faults and shear zones. *Geofluids*, 10(1–2), 217–233. <https://doi.org/10.1111/j.1468-8123.2010.00281.x>
- Cox, S. F., & Etheridge, M. A. (1983). Crack-seal fibre growth mechanisms and their significance in the development of oriented layer silicate microstructures. *Tectonophysics*, 92(1–3), 147–170. [https://doi.org/10.1016/0040-1951\(83\)90088-4](https://doi.org/10.1016/0040-1951(83)90088-4)
- Cross, A. J., Prior, D. J., Stipp, M., & Kidder, S. (2017). The recrystallized grain size piezometer for quartz: An EBSD-based calibration. *Geophysical Research Letters*, 44(13), 6667–6674. <https://doi.org/10.1002/2017gl073836>
- De Roo, J. A., & Weber, K. (1992). Laminated veins and hydrothermal breccia as markers of low-angle faulting, Rhenish Massif, Germany. *Tectonophysics*, 208(4), 413–430. [https://doi.org/10.1016/0040-1951\(92\)90438-c](https://doi.org/10.1016/0040-1951(92)90438-c)
- Drury, M. R., & Humphreys, F. J. (1988). Microstructural shear criteria associated with grain-boundary sliding during ductile deformation. *Journal of Structural Geology*, 10(1), 83–89. [https://doi.org/10.1016/0191-8141\(88\)90130-7](https://doi.org/10.1016/0191-8141(88)90130-7)
- Durney, D. W., & Ramsay, J. G. (1973). *Gravity and tectonics*. Wiley.
- Fagereng, Á., & Biggs, J. (2019). New perspectives on 'geological strain rates' calculated from both naturally deformed and actively deforming rocks. *Journal of Structural Geology*, 125, 100–110. <https://doi.org/10.1016/j.jsg.2018.10.004>
- Fagereng, Á., Remitti, F., & Sibson, R. H. (2010). Shear veins observed within anisotropic fabric at high angles to the maximum compressive stress. *Nature Geoscience*, 3(7), 482–485. <https://doi.org/10.1038/ngeo898>
- Fagereng, Á., Remitti, F., & Sibson, R. H. (2011). Incrementally developed slipenclaves — Geological record of repeating low stress-drop seismic events? *Tectonophysics*, 510(3), 381–386. <https://doi.org/10.1016/j.tecto.2011.08.015>
- Faleiros, F. M., da Cruz Campanha, G. A., da Silveira Bello, R. M., & Fuzikawa, K. (2010). Quartz recrystallization regimes, c-axis texture transitions and fluid inclusion reequilibration in a prograde greenschist to amphibolite facies mylonite zone (Ribeira Shear Zone, SE Brazil). *Tectonophysics*, 485(1–4), 193–214. <https://doi.org/10.1016/j.tecto.2009.12.014>
- Festa, A., Pini, G. A., Ogata, K., & Dilek, Y. (2019). Diagnostic features and field-criteria in recognition of tectonic, sedimentary and diapiric mélanges in orogenic belts and exhumed subduction-accretion complexes. *Gondwana Research*, 74, 7–30. <https://doi.org/10.1016/j.gr.2019.01.003>
- Finch, M. A., Weinberg, R. F., & Hunter, N. J. R. (2016). Water loss and the origin of thick ultramylonites. *Geology*, 44(8), 599–602. <https://doi.org/10.1130/g37972.1>
- Fisher, D. M., & Brantley, S. L. (1992). Models of quartz overgrowth and vein formation: Deformation and episodic fluid flow in an ancient subduction zone. *Journal of Geophysical Research*, 97(B13), 20043–20061. <https://doi.org/10.1029/92jb01582>
- Fliervoet, T. F., White, S. H., & Drury, M. R. (1997). Evidence for dominant grain-boundary sliding deformation in greenschist- and amphibolite-grade polymineralic ultramylonites from the Redbank Deformed Zone, Central Australia. *Journal of Structural Geology*, 19(12), 1495–1520. [https://doi.org/10.1016/s0191-8141\(97\)00076-x](https://doi.org/10.1016/s0191-8141(97)00076-x)
- Ganzhorn, A. C., Pilorgé, H., & Reynard, B. (2019). Porosity of metamorphic rocks and fluid migration within subduction interfaces. *Earth and Planetary Science Letters*, 522, 107–117. <https://doi.org/10.1016/j.epsl.2019.06.030>
- Gao, X., & Wang, K. (2017). Rheological separation of the megathrust seismogenic zone and episodic tremor and slip. *Nature*, 543(7645), 416–419. <https://doi.org/10.1038/nature21389>
- Gardner, R. L., Piazolo, S., & Daczko, N. R. (2016). Shape of pinch and swell structures as a viscosity indicator: Application to lower crustal polyphase rocks. *Journal of Structural Geology*, 88, 32–45. <https://doi.org/10.1016/j.jsg.2016.04.012>
- Gilgannon, J., Fusseis, F., Menegon, L., Regenauer-Lieb, K., & Buckman, J. (2017). Hierarchical creep cavity formation in an ultramylonite and implications for phase mixing. *Solid Earth*, 8(6), 1193–1209. <https://doi.org/10.5194/se-8-1193-2017>
- Giorgetti, G., Goffe, B., Memmi, I., & Nieto, F. (1998). Metamorphic evolution of Verrucano metasediments in Northern Apennines; new petrological constraints. *European Journal of Mineralogy*, 10(6), 1295–1308. <https://doi.org/10.1127/ejm/10/6/1295>
- Giuntoli, F., Menegon, L., & Warren, C. J. (2018). Replacement reactions and deformation by dissolution and precipitation processes in amphibolites. *Journal of Metamorphic Geology*, 36(9), 1263–1286. <https://doi.org/10.1111/jmg.12445>
- Giuntoli, F., Menegon, L., Warren, C. J., Darling, J., & Anderson, M. W. (2020). Protracted shearing at midcrustal conditions during large-scale thrusting in the Scandinavian Caledonides. *Tectonics*, 39(9), e2020TC006267. <https://doi.org/10.1029/2020TC006267>
- Giuntoli, F., & Viola, G. (2021). Cyclic brittle-ductile oscillations recorded in exhumed high-pressure continental units: A record of deep episodic tremor and slow slip events in the northern Apennines. *Geochemistry, Geophysics, Geosystems*, 22, e2021GC009805. <https://doi.org/10.1029/2021GC009805>
- Giuntoli, F., & Viola, G. (2022). A likely geological record of deep tremor and slow slip events from a subducted continental broken formation. *Scientific Reports*, 12(4506). <https://doi.org/10.1038/s41598-022-08489-2>
- Giuntoli, F., Viola, G., & Sørensen, B. E. (2022). Deformation mechanisms of blueschist facies continental metasediments may offer insights into deep episodic tremor and slow slip events [Dataset]. *Journal of Geophysical Research: Solid Earth*. Retrieved from <https://data.mendeley.com/datasets/d238p54v6g/2>
- Gomberg, J., & the Cascadia 2007 and Beyond Working Group. (2010). Slow-slip phenomena in Cascadia from 2007 and beyond: A review. *GSA Bulletin*, 122(7–8), 963–978. <https://doi.org/10.1130/B30287.1>
- Gosselin, J. M., Audet, P., Estève, C., McLellan, M., Mosher, S. G., & Schaeffer, A. J. (2020). Seismic evidence for megathrust fault-valve behavior during episodic tremor and slip. *Science Advances*, 6(4), eaay5174. <https://doi.org/10.1126/sciadv.aay5174>
- Hayman, N. W., & Lavier, L. L. (2014). The geologic record of deep episodic tremor and slip. *Geology*, 42(3), 195–198. <https://doi.org/10.1130/G34990.1>
- Hippert, J. F. (1994). Microstructures and c-axis fabrics indicative of quartz dissolution in sheared quartzites and phyllonites. *Tectonophysics*, 229(3), 141–163. [https://doi.org/10.1016/0040-1951\(94\)90026-4](https://doi.org/10.1016/0040-1951(94)90026-4)
- Hirth, G., Teyssier, C., & Dunlap, J. W. (2001). An evaluation of quartzite flow laws based on comparisons between experimentally and naturally deformed rocks. *International Journal of Earth Sciences*, 90, 77–87. <https://doi.org/10.1007/s005310000152>

- Hsü, K. J. (1968). Principles of melanges and their bearing on the Franciscan-Knoxville paradox. *The Geological Society of America Bulletin*, 79(8), 1063–1074.
- Hunter, N. J. R., Hasalová, P., Weinberg, R. F., & Wilson, C. J. L. (2016). Fabric controls on strain accommodation in naturally deformed mylonites: The influence of interconnected micaceous layers. *Journal of Structural Geology*, 83, 180–193. <https://doi.org/10.1016/j.jsg.2015.12.005>
- Ito, Y., & Obara, K. (2006). Very low frequency earthquakes within accretionary prisms are very low stress-drop earthquakes. *Geophysical Research Letters*, 33(9). <https://doi.org/10.1029/2006GL025883>
- Ito, Y., Obara, K., Shiomi, K., Sekine, S., & Hirose, H. (2007). Slow earthquakes coincident with episodic tremors and slow slip events. *Science*, 315(5811), 503–506. <https://doi.org/10.1126/science.1134454>
- Jaeger, J. C., & Cook, N. G. W. (1979). Fundamentals of rock mechanics.
- Jolivet, L., Faccenna, C., Goffé, B., Mattei, M., Rossetti, F., Brunet, C., et al. (1998). Midcrustal shear zones in postorogenic extension: Example from the northern Tyrrhenian Sea. *Journal of Geophysical Research*, 103(B6), 12123–12160. <https://doi.org/10.1029/97jb03616>
- Kato, A., Iidaka, T., Ikuta, R., Yoshida, Y., Katsumata, K., Iwasaki, T., et al. (2010). Variations of fluid pressure within the subducting oceanic crust and slow earthquakes. *Geophysical Research Letters*, 37(14), 1–5. <https://doi.org/10.1029/2010GL043723>
- Kerrick, R. (1976). Some effects of tectonic recrystallisation on fluid inclusions in vein quartz. *Contributions to Mineralogy and Petrology*, 59(2), 195–202. <https://doi.org/10.1007/bf00371308>
- Kilian, R., Heilbronner, R., & Stünitz, H. (2011). Quartz grain size reduction in a granitoid rock and the transition from dislocation to diffusion creep. *Journal of Structural Geology*, 33(8), 1265–1284. <https://doi.org/10.1016/j.jsg.2011.05.004>
- Kirkpatrick, J. D., Fagereng, Å., & Shelly, D. R. (2021). Geological constraints on the mechanisms of slow earthquakes. *Nature Reviews Earth & Environment*, 2, 285–301. <https://doi.org/10.1038/s43017-021-00148-w>
- Koehn, D., & Passchier, C. W. (2000). Shear sense indicators in striped bedding-veins. *Journal of Structural Geology*, 22(8), 1141–1151. [https://doi.org/10.1016/s0191-8141\(00\)00028-6](https://doi.org/10.1016/s0191-8141(00)00028-6)
- Kotowski, A. J., & Behr, W. M. (2019). Length scales and types of heterogeneities along the deep subduction interface: Insights from exhumed rocks on Syros Island, Greece. *Geosphere*, 15(4), 1038–1065. <https://doi.org/10.1130/ges02037.1>
- Kronenberg, A. K., Kirby, S. H., & Pinkston, J. (1990). Basal slip and mechanical anisotropy of biotite. *Journal of Geophysical Research*, 95(B12), 19257–19278. <https://doi.org/10.1029/jb095ib12p19257>
- Kushima, A., Qian, X., Zhao, P., Zhang, S., & Li, J. (2015). Ripplifications in van der Waals layers. *Nano Letters*, 15(2), 1302–1308. <https://doi.org/10.1021/nl5045082>
- Labaune, P., Berty, C., & Laurent, P. H. (1991). Syn-diagenetic evolution of shear structures in superficial nappes: An example from the northern Apennines (NW Italy). *Journal of Structural Geology*, 13(4), 385–398. [https://doi.org/10.1016/0191-8141\(91\)90012-8](https://doi.org/10.1016/0191-8141(91)90012-8)
- Lagoeiro, L., & Barbosa, P. (2010). Nucleation and growth of new grains in recrystallized quartz vein: An example from banded iron formation in Iron Quadrangle, Brazil. *Journal of Structural Geology*, 32(4), 595–604. <https://doi.org/10.1016/j.jsg.2010.03.007>
- Lazzarotto, A., Aldinucci, M., Cirilli, S., Costantini, A., Decandia, F. A., Pandeli, E., et al. (2003). Stratigraphic correlation of the Upper Palaeozoic-Triassic successions in southern Tuscany, Italy. *Bollettino Della Società Geologica Italiana, Special Volumes*, 2, 25–35.
- Lazzarotto, A., Mazzanti, R., & Mazzoncini, F. (1964). Geologia del promontorio Argentario (Grosseto) e del promontorio del Franco (Isola del Giglio-Grosseto). *Bollettino della Società Geologica Italiana*, 83(2), 1–124.
- Lingling, Y., Hiroo, K., & Thorne, L. (2021). Global variations of large megathrust earthquake rupture characteristics. *Science Advances*, 4(3), ea04915. <https://doi.org/10.1126/sciadv.a04915>
- Lloyd, G. E. (2004). Microstructural evolution in a mylonitic quartz simple shear zone: The significant roles of dauphine twinning and misorientation. *Geological Society, London, Special Publications*, 224(1), 39–61. <https://doi.org/10.1144/gsl.sp.2004.224.01.04>
- Lloyd, G. E., & Freeman, B. (1994). Dynamic recrystallization of quartz under greenschist conditions. *Journal of Structural Geology*, 16(6), 867–881. [https://doi.org/10.1016/0191-8141\(94\)90151-1](https://doi.org/10.1016/0191-8141(94)90151-1)
- Mainprice, D., Bachmann, F., Hielscher, R., & Schaeben, H. (2015). Descriptive tools for the analysis of texture projects with large datasets using MTEX: Strength, symmetry and components. *Geological Society, London, Special Publications*, 409(1), 251–271. <https://doi.org/10.1144/sp409.8>
- Malatesta, C., Federico, L., Crispini, L., & Capponi, G. (2018). Fluid-controlled deformation in blueschist-facies conditions: Plastic vs brittle behaviour in a brecciated mylonite (Voltri Massif, Western Alps, Italy). *Geological Magazine*, 155(2), 335–355. <https://doi.org/10.1017/s0016756816001163>
- Mares, V. M., & Kronenberg, A. K. (1993). Experimental deformation of muscovite. *Journal of Structural Geology*, 15(9–10), 1061–1075. [https://doi.org/10.1016/0191-8141\(93\)90156-5](https://doi.org/10.1016/0191-8141(93)90156-5)
- Mariani, E., Brodie, K. H., & Rutter, E. H. (2006). Experimental deformation of muscovite shear zones at high temperatures under hydrothermal conditions and the strength of phyllosilicate-bearing faults in nature. *Journal of Structural Geology*, 28(9), 1569–1587. <https://doi.org/10.1016/j.jsg.2006.06.009>
- Menegon, L., & Fagereng, Å. (2021). Tectonic pressure gradients during viscous creep drive fluid flow and brittle failure at the base of the seismogenic zone. *Geology*, 49(10), 1255–1259. <https://doi.org/10.1130/G49012.1>
- Menegon, L., Fusses, F., Stünitz, H., & Xiao, X. (2015). Creep cavitation bands control porosity and fluid flow in lower crustal shear zones. *Geology*, 43(3), 227–230. <https://doi.org/10.1130/g36307.1>
- Menegon, L., Pennacchioni, G., Heilbronner, R., & Pittarello, L. (2008). Evolution of quartz microstructure and c-axis crystallographic preferred orientation within ductilely deformed granitoids (Arolla unit, Western Alps). *Journal of Structural Geology*, 30(11), 1332–1347. <https://doi.org/10.1016/j.jsg.2008.07.007>
- Menegon, L., Pennacchioni, G., & Spiess, R. (2008). Dissolution-precipitation creep of K-feldspar in mid-crustal granite mylonites. *Journal of Structural Geology*, 30(5), 565–579. <https://doi.org/10.1016/j.jsg.2008.02.001>
- Menegon, L., Piazzolo, S., & Pennacchioni, G. (2011). The effect of Dauphiné twinning on plastic strain in quartz. *Contributions to Mineralogy and Petrology*, 161(4), 635–652. <https://doi.org/10.1007/s00410-010-0554-7>
- Molli, G. (2008). Northern Apennine–Corsica orogenic system: An updated overview. *Geological Society, London, Special Publications*, 298(1), 413–442. <https://doi.org/10.1144/sp298.19>
- Molli, G., Menegon, L., & Malasoma, A. (2017). Switching deformation mode and mechanisms during subduction of continental crust: A case study from Alpine Corsica. *Solid Earth*, 8(4), 767. <https://doi.org/10.5194/se-8-767-2017>
- Muñoz-Montecinos, J., Angiboust, S., Cambeses, A., & García-Casco, A. (2020). Multiple veining in a paleo-accretionary wedge: The metamorphic rock record of prograde dehydration and transient high pore-fluid pressures along the subduction interface (Western Series, central Chile). *Geosphere*, 16(3), 765–786. <https://doi.org/10.1130/GES02227.1>

- Muñoz-Montecinos, J., Angiboust, S., & Garcia-Casco, A. (2021). Blueschist-facies paleo-earthquakes in a serpentinite channel (Zagros suture, Iran) enlighten seismogenesis in Mariana-type subduction margins. *Earth and Planetary Science Letters*, 573, 117135. <https://doi.org/10.1016/j.epsl.2021.117135>
- Nakajima, J., & Uchida, N. (2018). Repeated drainage from megathrusts during episodic slow slip. *Nature Geoscience*, 11(5), 351–356. <https://doi.org/10.1038/s41561-018-0090-z>
- Neumann, B. (2000). Texture development of recrystallised quartz polycrystals unravelled by orientation and misorientation characteristics. *Journal of Structural Geology*, 22(11–12), 1695–1711. [https://doi.org/10.1016/s0191-8141\(00\)00060-2](https://doi.org/10.1016/s0191-8141(00)00060-2)
- Nishikawa, O., Saiki, K., & Wenk, H.-R. (2004). Intra-granular strains and grain boundary morphologies of dynamically recrystallized quartz aggregates in a mylonite. *Journal of Structural Geology*, 26(1), 127–141. [https://doi.org/10.1016/s0191-8141\(03\)00082-8](https://doi.org/10.1016/s0191-8141(03)00082-8)
- Obara, K. (2020). Characteristic activities of slow earthquakes in Japan. *Proceedings of the Japan Academy, Series B*, 96(7), 297–315. <https://doi.org/10.2183/pjab.96.022>
- Obara, K., & Kato, A. (2016). Connecting slow earthquakes to huge earthquakes. *Science*, 353(6296), 253–257. <https://doi.org/10.1126/science.aaf1512>
- Okamoto, A. S., Verberne, B. A., Niemeijer, A. R., Takahashi, M., Shimizu, I., Ueda, T., & Spiers, C. J. (2019). Frictional properties of simulated chlorite gouge at hydrothermal conditions: Implications for subduction megathrusts. *Journal of Geophysical Research: Solid Earth*, 124(5), 4545–4565. <https://doi.org/10.1029/2018jb017205>
- Peccerillo, A. (2005). *Plio-quadernary volcanism in Italy* (Vol. 365). Springer.
- Pennacchioni, G., Menegon, L., Leiss, B., Nestola, F., & Bromiley, G. (2010). Development of crystallographic preferred orientation and microstructure during plastic deformation of natural coarse-grained quartz veins. *Journal of Geophysical Research*, 115(B12). <https://doi.org/10.1029/2010JB007674>
- Pfiffner, O. A., & Ramsay, J. G. (1982). Constraints on geological strain rates; arguments from finite strain states of naturally deformed rocks. *Journal of Geophysical Research*, 87(B1), 311–321. <https://doi.org/10.1029/JB087iB01p00311>
- Platt, J. P., Xia, H., & Schmidt, W. L. (2018). Rheology and stress in subduction zones around the aseismic/seismic transition. *Progress in Earth and Planetary Science*, 5(1), 24. <https://doi.org/10.1186/s40645-018-0183-8>
- Price, N. A., Song, W. J., Johnson, S. E., Gerbi, C. C., Beane, R. J., & West, D. P. (2016). Recrystallization fabrics of sheared quartz veins with a strong pre-existing crystallographic preferred orientation from a seismogenic shear zone. *Tectonophysics*, 682, 214–236. <https://doi.org/10.1016/j.tecto.2016.05.030>
- Prior, D. J., Wheeler, J., Peruzzo, L., Spiess, R., & Storey, C. (2002). Some garnet microstructures: An illustration of the potential of orientation maps and misorientation analysis in microstructural studies. *Journal of Structural Geology*, 24(6–7), 999–1011. [https://doi.org/10.1016/S0191-8141\(01\)00087-6](https://doi.org/10.1016/S0191-8141(01)00087-6)
- Raimbourg, H., Rajič, K., Moris-Muttoni, B., Famin, V., Palazzin, G., Fisher, D., et al. (2021). Quartz vein geochemistry records deformation processes in convergent zones. *Geochemistry, Geophysics, Geosystems*, 22(4), e2020GC009201. <https://doi.org/10.1029/2020GC009201>
- Ramsay, J. G. (1980). The crack–seal mechanism of rock deformation. *Nature*, 284(5752), 135–139. <https://doi.org/10.1038/284135a0>
- Rossetti, F., Faccenna, C., Jolivet, L., Funicello, R., Tecce, F., & Brunet, C. (1999). Syn-versus post-orogenic extension: The case study of Giglio island (northern Tyrrhenian Sea, Italy). *Tectonophysics*, 304(1–2), 71–93. [https://doi.org/10.1016/s0040-1951\(98\)00304-7](https://doi.org/10.1016/s0040-1951(98)00304-7)
- Ryan, E., Papeschi, S., Viola, G., Musumeci, G., Mazzarini, F., Torgersen, E., et al. (2021). Syn-orogenic exhumation of high-P units by upward extrusion in an accretionary wedge: Insights from the eastern Elba Nappe Stack (northern Apennines, Italy). *Tectonics*, 40(5), e2020TC006348. <https://doi.org/10.1029/2020TC006348>
- Saffer, D. M., & Tobin, H. J. (2011). Hydrogeology and mechanics of subduction zone forearcs: Fluid flow and pore pressure. *Annual Review of Earth and Planetary Sciences*, 39(1), 157–186. <https://doi.org/10.1146/annurev-earth-040610-133408>
- Schmidt, D. A., & Gao, H. (2010). Source parameters and time-dependent slip distributions of slow slip events on the Cascadia subduction zone from 1998 to 2008. *Journal of Geophysical Research*, 115(B4). <https://doi.org/10.1029/2008JB006045>
- Schmidt, W. L., & Platt, J. P. (2022). Stress, microstructure, and deformation mechanisms during subduction underplating at the depth of tremor and slow slip, Franciscan Complex, northern California. *Journal of Structural Geology*, 154, 104469. <https://doi.org/10.1016/j.jsg.2021.104469>
- Shea, W. T., & Kronenberg, A. K. (1993). Strength and anisotropy of foliated rocks with varied mica contents. *Journal of Structural Geology*, 15(9–10), 1097–1121. [https://doi.org/10.1016/0191-8141\(93\)90158-7](https://doi.org/10.1016/0191-8141(93)90158-7)
- Sibson, R. H. (1990). Conditions for fault-valve behaviour. *Geological Society, London, Special Publications*, 54(1), 15–28. <https://doi.org/10.1144/gsl.sp.1990.054.01.02>
- Sibson, R. H. (2013). Stress switching in subduction forearcs: Implications for overpressure containment and strength cycling on megathrusts. *Tectonophysics*, 600, 142–152. <https://doi.org/10.1016/j.tecto.2013.02.035>
- Sivakugan, N., Das, B. M., Lovisa, J., & Patra, C. R. (2014). Determination of c and ϕ of rocks from indirect tensile strength and uniaxial compression tests. *International Journal of Geotechnical Engineering*, 8(1), 59–65. <https://doi.org/10.1179/1938636213z.00000000053>
- Sørensen, B. E., Hjelen, J., Ånes, H. W., & Breivik, T. (2020). Recent features in EBSD, including new trapezoidal correction for multi-mapping. In *IOP conference series: Materials science and engineering* (Vol. 891, p. 12021). IOP Publishing.
- Spruzeniece, L., Piazzolo, S., & Maynard-Casely, H. E. (2017). Deformation-resembling microstructure created by fluid-mediated dissolution–precipitation reactions. *Nature Communications*, 8, 14032. <https://doi.org/10.1038/ncomms14032>
- Stipp, M., Stünitz, H., Heilbronner, R., & Schmid, S. M. (2002a). Dynamic recrystallization of quartz: Correlation between natural and experimental conditions. *Geological Society, London, Special Publications*, 200(1), 171–190. <https://doi.org/10.1144/gsl.sp.2001.200.01.11>
- Stipp, M., Stünitz, H., Heilbronner, R., & Schmid, S. M. (2002b). The eastern Tonale fault zone: A ‘natural laboratory’ for crystal plastic deformation of quartz over a temperature range from 250 to 700 C. *Journal of Structural Geology*, 24(12), 1861–1884. [https://doi.org/10.1016/s0191-8141\(02\)00035-4](https://doi.org/10.1016/s0191-8141(02)00035-4)
- Stöckhert, B., Wachmann, M., Küster, M., & Bimmermann, S. (1999). Low effective viscosity during high pressure metamorphism due to dissolution precipitation creep: The record of HP–LT metamorphic carbonates and siliciclastic rocks from Crete. *Tectonophysics*, 303(1–4), 299–319.
- Takahashi, N., Kodaira, S., Nakanishi, A., Park, J.-O., Miura, S., Tsuru, T., et al. (2002). Seismic structure of Western end of the Nankai trough seismogenic zone. *Journal of Geophysical Research*, 107(B10), ESE 2-1–ESE 2-19. <https://doi.org/10.1029/2000JB000121>
- Treppmann, C. A., Lenze, A., & Stöckhert, B. (2010). Static recrystallization of vein quartz pebbles in a high-pressure–low-temperature metamorphic conglomerate. *Journal of Structural Geology*, 32(2), 202–215. <https://doi.org/10.1016/j.jsg.2009.11.005>
- Treppmann, C. A., & Seybold, L. (2019). Deformation at low and high stress-loading rates. *Geoscience Frontiers*, 10(1), 43–54. <https://doi.org/10.1016/j.gsf.2018.05.002>

- Treppmann, C. A., Stöckhert, B., Dörner, D., Moghadam, R. H., Küster, M., & Röller, K. (2007). Simulating coseismic deformation of quartz in the middle crust and fabric evolution during postseismic stress relaxation—An experimental study. *Tectonophysics*, *442*(1–4), 83–104. <https://doi.org/10.1016/j.tecto.2007.05.005>
- Trimby, P. W., Prior, D. J., & Wheeler, J. (1998). Grain boundary hierarchy development in a quartz mylonite. *Journal of Structural Geology*, *20*(7), 917–935. [https://doi.org/10.1016/s0191-8141\(98\)00026-1](https://doi.org/10.1016/s0191-8141(98)00026-1)
- Ujii, K., Saishu, H., Fagereng, Å., Nishiyama, N., Otsubo, M., Masuyama, H., & Kagi, H. (2018). An explanation of episodic tremor and slow slip constrained by crack-seal veins and viscous shear in subduction Mélanges. *Geophysical Research Letters*, *45*(11), 5371–5379. <https://doi.org/10.1029/2018GL078374>
- Urai, J. L., Means, W. D., & Lister, G. S. (1986). Dynamic recrystallization of minerals. In B. Hobbs & H. Heard (Eds.), *Mineral and rock deformation* (pp. 1–43). <https://doi.org/10.1029/GM036p0161>
- Viegas, G., Menegon, L., & Archanjo, C. (2016). Brittle grain-size reduction of feldspar, phase mixing and strain localization in granitoids at mid-crustal conditions (Pernambuco shear zone, NE Brazil). *Solid Earth*, *7*(2), 375–396. <https://doi.org/10.5194/se-7-375-2016>
- Vignaroli, G., Faccenna, C., Rossetti, F., & Jolivet, L. (2009). Insights from the Apennines metamorphic complexes and their bearing on the kinematics evolution of the orogen. *Geological Society, London, Special Publications*, *311*, 235–256. <https://doi.org/10.1144/sp311.9>
- Wallace, L. M., & Beavan, J. (2010). Diverse slow slip behavior at the Hikurangi subduction margin, New Zealand. *Journal of Geophysical Research*, *115*(B12). <https://doi.org/10.1029/2010jb007717>
- Warren-Smith, E., Fry, B., Wallace, L., Chon, E., Henrys, S., Sheehan, A., et al. (2019). Episodic stress and fluid pressure cycling in subducting oceanic crust during slow slip. *Nature Geoscience*, *12*(6), 475–481. <https://doi.org/10.1038/s41561-019-0367-x>
- Wells, D. L., & Coppersmith, K. J. (1994). New empirical relationships among magnitude, rupture length, rupture width, rupture area, and surface displacement. *Bulletin of the Seismological Society of America*, *84*(4), 974–1002.
- Westerman, D. S., Innocenti, F., Tonarini, S., & Ferrara, G. (1993). The Pliocene intrusions of the island of Giglio. *Memorie della Società Geologica Italiana*, *49*, 345–363.
- Wheeler, J., Prior, D. J., Jiang, Z., Spiess, R., & Trimby, P. W. (2001). The petrological significance of misorientations between grains. *Contributions to Mineralogy and Petrology*, *141*(1), 109–124. <https://doi.org/10.1007/s004100000225>
- White, S. (1977). Geological significance of recovery and recrystallization processes in quartz. *Tectonophysics*, *39*(1–3), 143–170. [https://doi.org/10.1016/0040-1951\(77\)90093-2](https://doi.org/10.1016/0040-1951(77)90093-2)
- Whitney, D. L., & Evans, B. W. (2010). Abbreviations for names of rock-forming minerals. *American Mineralogist*, *95*(1), 185–187. <https://doi.org/10.2138/am.2010.3371>
- Wintsch, R. P., Christoffersen, R., & Kronenberg, A. K. (1995). Fluid-rock reaction weakening of fault zones. *Journal of Geophysical Research*, *100*(B7), 13021–13032. <https://doi.org/10.1029/94jb02622>
- Wintsch, R. P., & Yi, K. (2002). Dissolution and replacement creep: A significant deformation mechanism in mid-crustal rocks. *Journal of Structural Geology*, *24*(6), 1179–1193. [https://doi.org/10.1016/s0191-8141\(01\)00100-6](https://doi.org/10.1016/s0191-8141(01)00100-6)
- Wright, S. I., Nowell, M. M., & Field, D. P. (2011). A review of strain analysis using electron backscatter diffraction. *Microscopy and Microanalysis*, *17*(3), 316–329. <https://doi.org/10.1017/S1431927611000055>
- Zhang, X.-P., Wong, L. N. Y., Wang, S.-J., & Han, G.-Y. (2011). Engineering properties of quartz mica schist. *Engineering Geology*, *121*(3–4), 135–149. <https://doi.org/10.1016/j.enggeo.2011.04.020>